THE DYNAMIC EVOLUTION OF TWISTED MAGNETIC FLUX TUBES IN A THREE-DIMENSIONAL CONVECTING FLOW. II. TURBULENT PUMPING AND THE COHESION OF Ω-LOOPS

W. P. ABBETT,[1,2] G. H. FISHER,[1,2] Y. FAN,[2,3] AND D. J. BERCIK[1]

ABSTRACT

We present a set of three-dimensional MHD simulations using the anelastic approximation of active region–scale flux ropes embedded in a turbulent, stratified model convection zone. We simulate the evolution of Ω-loops and other magnetic structures of varying field strengths, helicities, and morphologies in both rotating and nonrotating background states. We show that if the magnetic energy of a flux tube is weak relative to the kinetic energy density of strong downdrafts, convective flows dominate the evolution, flux tubes of any shape rapidly lose cohesion, and the magnetic field redistributes itself throughout the domain over timescales characteristic of convective turnover. We determine the conditions under which magnetic tension resulting from field line twist can provide the force necessary to prevent a relatively weak flux tube from losing cohesion during its ascent through the turbulent convection zone. Our simulations show that there is no initial tendency for a horizontal magnetic flux tube or layer to be preferentially transported in one vertical direction over the other solely as a result of the presence of an asymmetric vertical flow field. However, as the simulations progress, there is a transient net transport of magnetic flux into the lower half of the computational domain as the distribution of the magnetic field changes and flux is expelled from cell centers into converging downflows and intergranular lanes. This pumping mechanism is weak and uncorrelated with the degree of vertical flow asymmetry. We find that the strong turbulent pumping evident in simulations of penetrative convection—the efficient transport of magnetic flux to the base of the convection zone over several local turnover times—does not manifest itself in a closed domain in the absence of a convective overshoot layer. Thus, we suggest that this rapid redistribution of flux is primarily due to the penetration of magnetic flux into the stable layer where it remains over a timescale that far exceeds that of convective turnover. We also find that different treatments of the viscosity of a Newtonian fluid—in which the coefficient of either kinematic or dynamic viscosity is held constant throughout the domain—do not affect the global average evolution of embedded magnetic structures, although the details of the evolution may differ between models.

Subject headings: methods: numerical — MHD — Sun: interior — Sun: magnetic fields

1. INTRODUCTION

The strong magnetic field observed in and around sunspots is widely believed to originate via a dynamo mechanism at or near the base of the solar convection zone. If so, magnetic flux must be transported through the convection zone in such a way as to exhibit the familiar structures and characteristics of active regions observed at the solar surface and described by such empirical relations as Hale's polarity law (Hale et al. 1919) and Joy's law (see Zirin 1988, p. 307; Fisher et al. 1995). One way to characterize the observations is to assume that magnetic flux rises buoyantly through the interior in the form of discrete tubes and that these tubes do not fragment during their ascent through the convection zone (assumptions implicit in the "thin flux tube" formulation of Spruit 1981; Caligari et al. 1995; Fan & Fisher 1996; Longcope et al. 1998). Recent three-dimensional numerical simulations of the dynamic subsurface evolution of magnetic flux ropes (Abbett et al. 2000, 2001) test this assumption and show that in contrast to two-dimensional axisymmetric models (see Longcope

et al. 1996), weakly twisted flux tubes that form near the base of a nonturbulent model convection zone can indeed rise through the entirety of the stratified interior without breaking apart into counterrotating fragments.

However, with the exception of Dorch et al. (2001) and Fan et al. (2003, hereafter Paper I), multidimensional models ignore the effects of turbulent flow by modeling the rise of flux tubes in static, adiabatically stratified model convection zones. This approach implicitly assumes that the magnetic field strength of a tube is sufficient to overcome the dynamic influence of convective flows. Although this is likely the case for Ω-loops that are the progenitors of strong active regions, there are many regions of interest where emerging or submerging magnetic fields can be weak relative to the kinetic energy density of surrounding flows—ephemeral regions, the small-scale "salt and pepper" magnetic elements present in quiescent regions, and the magnetic features in and around decaying active regions, to name a few. In such cases, the influence of convection on the evolution of magnetic structures cannot be ignored.

In this paper, we perform a large number of three-dimensional MHD simulations (in the anelastic approximation) of magnetic flux ropes embedded in a turbulent stratified model convection zone to characterize the effect of convective flows on the subsurface evolution of active region–scale magnetic structures. We extend the recent results of Paper I to Ω-loops of varying magnetic field strengths, helicities, and

[1] Space Sciences Laboratory, University of California, 7 Gauss Way, Berkeley, CA 94720-7450.
[2] Kavli Institute for Theoretical Physics, Kohn Hall, University of California, Santa Barbara, CA 93106-4030.
[3] High Altitude Observatory, National Center for Atmospheric Research, 3450 Mitchell Lane, Boulder, CO 80301. The National Center for Atmospheric Research is sponsored by the National Science Foundation.

morphologies in both rotating and nonrotating convective background states and determine how different treatments of viscosity affect our results. The remainder of the paper is organized as follows: In § 2 we introduce the anelastic approximation and describe how each model convection zone is generated; in § 3.1 we characterize the decay of a relatively weak flux rope as it interacts with convective flows; in § 3.2 we offer an interpretation of weak turbulent pumping—the net transport of magnetic flux into or out of the lower half of the model convection zone; in § 3.3 we characterize the effects of field line twist on the cohesion of a buoyant Ω-loop embedded in a turbulent model convection zone; and in § 4 we discuss the implications of our results. Finally, in § 5 we summarize our findings.

2. METHOD

The anelastic approximation (Ogura & Phillips 1962; Gough 1969) results from a scaled variable expansion of the three-dimensional compressible MHD equations about a nearly adiabatically stratified plane-parallel reference atmosphere (which we take to be a polytrope). The time-derivative term in the continuity equation is of sufficiently high order in the expansion that it can be neglected, thereby filtering out fast-moving acoustic waves from the calculation. This approximation is well suited for simulations of subsonic processes in the high-β plasma deep in the solar convection zone, and the inherent computational savings allow for a large exploration of parameter space. We numerically solve a nondimensional form of the following anelastic equations in a rotating Cartesian reference frame:

$$\nabla \cdot (\rho_0 \boldsymbol{v}) = 0, \tag{1}$$

$$\rho_0 \left[\frac{\partial \boldsymbol{v}}{\partial t} + (\boldsymbol{v} \cdot \nabla)\boldsymbol{v} \right] = -\nabla p_1 + \rho_1 \boldsymbol{g} - 2\rho_0 (\boldsymbol{\Omega} \times \boldsymbol{v})$$
$$+ \frac{1}{4\pi} (\nabla \times \boldsymbol{B}) \times \boldsymbol{B} + \nabla \cdot \Pi, \tag{2}$$

$$\rho_0 T_0 \left[\frac{\partial s_1}{\partial t} + (\boldsymbol{v} \cdot \nabla)(s_0 + s_1) \right] = \nabla \cdot (K \rho_0 T_0 \nabla s_1)$$
$$+ \frac{\eta}{4\pi} |\nabla \times \boldsymbol{B}|^2 + (\Pi \cdot \nabla) \cdot \boldsymbol{v}, \tag{3}$$

$$\nabla \cdot \boldsymbol{B} = 0, \tag{4}$$

$$\frac{\partial \boldsymbol{B}}{\partial t} = \nabla \times (\boldsymbol{v} \times \boldsymbol{B}) - \nabla \times (\eta \nabla \times \boldsymbol{B}), \tag{5}$$

$$\frac{\rho_1}{\rho_0} = \frac{p_1}{p_0} - \frac{T_1}{T_0}, \tag{6}$$

$$\frac{s_1}{c_p} = \frac{T_1}{T_0} - \frac{\gamma - 1}{\gamma} \frac{p_1}{p_0}. \tag{7}$$

Here ρ_1, p_1, T_1, s_1, $\boldsymbol{v}$, and $\boldsymbol{B}$ refer to the density, gas pressure, temperature, entropy, velocity, and magnetic field perturbations, and ρ_0, p_0, T_0, and s_0 denote the corresponding values of the reference state, taken to be a field-free, nearly adiabatically stratified polytrope of index $m = 1.5$ [related to γ by $m = 1/(\gamma - 1)$]. The gravitational acceleration, $\boldsymbol{g} = -g\hat{\boldsymbol{z}}$, is assumed uniform, and c_p, η, and K refer to the specific heat at constant pressure and the coefficients of magnetic and thermal diffusion, respectively. The viscous stress tensor is given by $\Pi_{ij} \equiv \mu[\partial v_i/\partial x_j + \partial v_j/\partial x_i - 2/3(\nabla \cdot \boldsymbol{v})\delta_{ij}]$, where μ is the

coefficient of dynamic viscosity and δ_{ij} is the Kronecker delta function.

This system of equations is identical to the system solved in Paper I, except for the addition of the Coriolis term to the momentum equation (eq. [2]). The angular velocity about the Sun's axis, $\boldsymbol{\Omega}$, is assumed constant throughout the domain, and rotation is treated using the modified *f*-plane approximation of Brummell et al. (1996). Boundaries are assumed periodic in the horizontal directions and nonpenetrating and stress-free at the top and bottom of the box. A detailed derivation of the above system of equations can be found in Lantz & Fan (1999 and references therein), and the numerical techniques used to solve equations (1)–(7) are briefly summarized in Paper I and described in full in Fan et al. (1999) and Abbett et al. (2001). We note that unlike, e.g., Tobias et al. (2001), Dorch & Nordlund (2001), Brummell et al. (2002), and Ossendrijver et al. (2002), our models do not include a convectively stable overshoot layer below the model convection zone.

We generate a number of distinct field-free convective states. In each case, convection is initiated by a small random entropy perturbation within the computational domain, and the simulations progress until the model convection zone is thermally relaxed. We relax states in both the presence and absence of rotation and with two standard treatments of the viscosity of a Newtonian fluid: the first assumes a constant coefficient of kinematic viscosity as a function of depth (ν), and the second, a constant dynamic viscosity ($\mu = \rho_0 \nu$). For the runs for which ν is held constant, the coefficient of thermal diffusion is also assumed constant; for the runs for which μ is held constant, $\rho_0 K$ is assumed constant.

Buoyant magnetic flux tubes with varying amounts of initial twist are inserted near the base of the field-free turbulent domain; as in Paper I, their initial field is given by

$$\boldsymbol{B} = B_x(r)\hat{\boldsymbol{x}} + B_\theta(r)\hat{\boldsymbol{\theta}}, \tag{8}$$

where

$$B_x(r) \equiv B_0 e^{-r^2/a^2}, \tag{9}$$

$$B_\theta(r) = \frac{q}{a} r B_x(r). \tag{10}$$

Here r refers to the radial distance to the tube's central axis, θ denotes the azimuthal direction, and q represents a dimensionless measure of the amount of field line twist. Tables 1–4 list each simulation and their associated parameters. The nondimensional parameters Re, Re$_m$, Pr, and Ro denote the Reynolds number, magnetic Reynolds number, Prandtl number, and Rossby number, respectively, and are given by Re $\equiv v_c H_r/\nu$, Re$_m \equiv v_c H_r/\eta$, Pr $\equiv \nu/K$, and Ro $\equiv v_c/(2\Omega H_r)$. The velocity scale v_c is given by $v_c \equiv (\alpha \delta_r g H_r)^{1/2}$, where H_r and δ_r denote the pressure scale height and the nondimensional superadiabaticity (assumed small) at the base of the domain. The coefficient α is a parameter in the code used to control the value of s_0 at the top boundary ($\alpha = 1$ when μ is held constant, and $\alpha = 8$ when ν is held constant, to ensure that the total entropy drop is identical for the two convective states). The parameters that define the initial state of the tube are B_0/B_{eq}, a/H_r, and q: the magnitude of the tube's axial field relative to the equipartition field strength [taken with respect to the kinetic energy density of strong downdrafts, $B_{eq} = (4\pi\rho_r)^{1/2} v_c$], the radius of the tube (in units of a pressure scale height at the base of the computational

TABLE 1
INITIAL STATES AND REFERENCE SIMULATIONS

Label	Grid (x, y, z)	$\dfrac{B_0}{B_{eq}}$	q	$\dfrac{a}{H_r}$	$Re \equiv \dfrac{v_c H_r}{\nu}$	$Re_m \equiv \dfrac{v_c H_r}{\eta}$	$Pr \equiv \dfrac{\nu}{K}$	$Ro \equiv \dfrac{v_c}{2\Omega H_r}$	Viscosity[a]
I1	$288 \times 288 \times 72$	...	...	...	300.0	...	0.5	∞	ν_0
I2	$288 \times 288 \times 72$	...	...	...	750.0	...	1.0	∞	μ_0
I3	$288 \times 288 \times 72$	...	...	...	300.0	...	0.5	1	ν_0
R1[b]	$288 \times 288 \times 72$	1.0	0.0	0.21	3500.0	3500.0	1.0	∞	μ_0
R2[c]..........	$288 \times 288 \times 72$	1.0	0.0	0.21	3500.0	3500.0	1.0	∞	μ_0

[a] Whether the coefficient of kinematic or dynamic viscosity is held constant.
[b] Neutrally buoyant tube in a nonturbulent, adiabatically stratified model convection zone.
[c] Buoyant tube in a nonturbulent, adiabatically stratified model convection zone.

TABLE 2
SIMULATIONS OF NEUTRALLY BUOYANT FLUX TUBES/LAYERS IN A CONVECTING BACKGROUND

Label	Grid (x, y, z)	$\dfrac{B_0}{B_{eq}}$	q	$\dfrac{a}{H_r}$	$Re \equiv \dfrac{v_c H_r}{\nu}$	$Re_m \equiv \dfrac{v_c H_r}{\eta}$	$Pr \equiv \dfrac{\nu}{K}$	$Ro \equiv \dfrac{v_c}{2\Omega H_r}$	Viscosity[a]
H1...........	$288 \times 288 \times 72$	1.0	0.0	0.21	750.0	3500.0	1.0	∞	μ_0
H2...........	$288 \times 288 \times 72$	2.0	0.0	0.21	750.0	3500.0	1.0	∞	μ_0
H3...........	$288 \times 288 \times 72$	2.0	0.0	0.21	300.0	3500.0	0.5	∞	ν_0
H4...........	$288 \times 288 \times 72$	0.1	0.0	0.21	750.0	750.0	1.0	∞	μ_0
H5...........	$288 \times 288 \times 72$	0.1	0.0	0.21	300.0	300.0	0.5	∞	ν_0
H6[b]	$288 \times 288 \times 72$	0.1	...	...	750.0	750.0	1.0	∞	μ_0
H7[b]	$288 \times 288 \times 72$	0.1	...	...	300.0	300.0	0.5	∞	ν_0
H8[b]	$288 \times 288 \times 72$	0.1	...	...	300.0	200.0	0.5	∞	ν_0
H9[b]	$288 \times 288 \times 72$	0.01	...	...	750.0	750.0	1.0	∞	μ_0
H10[b]	$288 \times 288 \times 72$	0.01	...	...	300.0	300.0	0.5	∞	ν_0

[a] Whether the coefficient of kinematic or dynamic viscosity is held constant.
[b] Runs initialized with a thin horizontal slab of magnetic field placed at the center of the box.

TABLE 3
SIMULATIONS OVER LONG TIME INTERVALS

Label	Grid (x, y, z)	$\dfrac{B_0}{B_{eq}}$	q	$\dfrac{a}{H_r}$	$Re \equiv \dfrac{v_c H_r}{\nu}$	$Re_m \equiv \dfrac{v_c H_r}{\eta}$	$Pr \equiv \dfrac{\nu}{K}$	$Ro \equiv \dfrac{v_c}{2\Omega H_r}$	Viscosity[a]
LT1	$288 \times 288 \times 72$	1.0	0.0	0.21	750.0	1500.0	1.0	∞	μ_0
LT2[b]	$288 \times 288 \times 72$	5×10^{-2}	...	...	750.0	1500.0	1.0	∞	μ_0
LT3[c]........	$288 \times 288 \times 72$	10^{-2}	...	...	750.0	1500.0	1.0	∞	μ_0
LT4[c]........	$288 \times 288 \times 72$	10^{-4}	...	...	750.0	1500.0	1.0	∞	μ_0

[a] Whether the coefficient of kinematic or dynamic viscosity is held constant.
[b] Runs initialized with a thin horizontal slab of magnetic field placed at the center of the box.
[c] Runs initialized with a horizontal magnetic field permeating the entirety of the box.

TABLE 4
SIMULATIONS OF BUOYANT FLUX TUBES IN A CONVECTING BACKGROUND

Label (1)	Grid (x, y, z) (2)	$\frac{B_0}{B_{eq}}$ (3)	q (4)	$\frac{a}{H_r}$ (5)	Loop[a] (6)	$Re \equiv \frac{v_c H_r}{\nu}$ (7)	$Re_m \equiv \frac{v_c H_r}{\eta}$ (8)	$Pr \equiv \frac{\nu}{K}$ (9)	$Ro \equiv \frac{v_c}{2\Omega H_r}$ (10)	Viscosity[b] (11)
A1............	$288 \times 288 \times 72$	1.0	0.0	0.21	No	750.0	3500.0	1.0	∞	μ_0
A2............	$288 \times 288 \times 72$	3.0	0.0	0.21	No	750.0	3500.0	1.0	∞	μ_0
A3............	$288 \times 288 \times 72$	5.0	0.0	0.21	No	750.0	3500.0	1.0	∞	μ_0
A4............	$288 \times 288 \times 72$	1.0	0.0	0.21	No	750.0	5000.0	1.0	∞	μ_0
A5............	$288 \times 288 \times 72$	3.0	0.0	0.21	No	750.0	5000.0	1.0	∞	μ_0
B1...........	$288 \times 288 \times 72$	1.0	0.0	0.21	No	300.0	3500.0	0.5	∞	ν_0
B2...........	$288 \times 288 \times 72$	3.0	0.0	0.21	No	300.0	3500.0	0.5	∞	ν_0
B3...........	$256 \times 256 \times 60$	5.0	0.0	0.25	No	260.0	5000.0	1.0	∞	ν_0
B4[c]........	$288 \times 288 \times 72$	2.0	0.0	0.21	No	300.0	3500.0	0.5	∞	ν_0
C1...........	$256 \times 256 \times 60$	3.0	0.0	0.25	Yes	750.0	5000.0	1.0	∞	μ_0
C2...........	$256 \times 256 \times 60$	5.0	0.0	0.25	Yes	750.0	5000.0	1.0	∞	μ_0
C3...........	$256 \times 256 \times 60$	10.0	0.0	0.25	Yes	750.0	3500.0	1.0	∞	μ_0
D1...........	$256 \times 256 \times 60$	1.0	0.0	0.25	Yes	260.0	3500.0	1.0	∞	ν_0
D2...........	$256 \times 256 \times 60$	3.0	0.0	0.25	Yes	260.0	5000.0	1.0	∞	ν_0
D3...........	$256 \times 256 \times 60$	5.0	0.0	0.25	Yes	260.0	5000.0	1.0	∞	ν_0
E1	$288 \times 288 \times 72$	1.5	0.125	0.21	Yes	750.0	1500.0	1.0	∞	μ_0
E2	$288 \times 288 \times 72$	3.0	0.125	0.21	Yes	750.0	1500.0	1.0	∞	μ_0
E3	$288 \times 288 \times 72$	1.5	0.250	0.21	Yes	750.0	3500.0	1.0	∞	μ_0
E4	$288 \times 288 \times 72$	3.0	0.250	0.21	Yes	750.0	1500.0	1.0	∞	μ_0
F1	$256 \times 256 \times 60$	2.0	0.0	0.25	Yes	275.0	3500.0	1.0	1.0	ν_0
F2	$256 \times 256 \times 60$	3.0	0.0	0.25	Yes	275.0	5000.0	1.0	1.0	ν_0
F3	$256 \times 256 \times 60$	5.0	0.0	0.25	Yes	275.0	5000.0	1.0	1.0	ν_0
F4	$256 \times 256 \times 60$	10.0	0.0	0.25	Yes	275.0	5000.0	1.0	1.0	ν_0
G1[d].........	$288 \times 288 \times 72$	2.0	...	...	...	750.0	1500.0	1.0	1.0	μ_0
G2[d].........	$288 \times 288 \times 72$	2.0	...	...	...	750.0	1500.0	1.0	1.0	μ_0

[a] Whether an initial entropy perturbation was applied to the flux tube so that the ends of the tube are neutrally buoyant, allowing the tube to rise as a classical Ω-loop.

[b] Whether the coefficient of kinematic or dynamic viscosity is held constant.

[c] Initial horizontal flux tube positioned off-center at $(y, z) = (72, 13)$.

[d] Runs G1 and G2 are initialized with a thin slab of magnetic field placed near the base of the box and oriented parallel to the east-west direction. The box of run G1 is positioned at $15°$ latitude (as are runs F1–F4), while the box of run G2 is positioned at $60°$ latitude for comparison.

box), and the amount of field line twist along the tube. The additional parameter "loop" (Table 4, col. [6]) indicates whether or not an additional entropy perturbation was applied along the axis of the initial tube such that only the ends of the tube are neutrally buoyant. This perturbation facilitates the formation of an Ω-shaped structure without performing the computationally expensive step of evolving each flux tube from a state of force balance (e.g., Caligari et al. 1995; Fan & Fisher 1996; Fan 2001).

3. RESULTS

Figure 1 shows two of the initial field-free, nonrotating convective states (runs I1 and I2 of Table 1). We generate these distinct, thermally relaxed initial states so that we can determine how our different treatments of viscosity affect the results of a given calculation. The images in Figure 1 (left) are horizontal slices taken from the simulation in which the coefficient of dynamic viscosity μ is held constant, and the images in Figure 1 (right) are from the simulation in which the coefficient of kinematic viscosity ν is held constant. Figure 1 (top) shows slices from each simulation near the top of the domain; Figure 1 (bottom) shows slices closer to the lower boundary. In each run, the coefficients are set to the lowest value possible without introducing excessive numerical noise into the calculation.

The resolution of the Cartesian domain is $288 \times 288 \times 72$, which gives a 4:4:1 aspect ratio for the box. The density dependence of the dimensionless Reynolds number ($Re \equiv$ $v_c H_r/\nu$) is evident in Figure 1 (left), where $\mu = \rho_0 \nu$ is held constant. Here the effective Reynolds number increases with depth, and the base of the domain is more turbulent than the surface layers. Conversely, when ν is held constant (Fig. 1, right), increased structure is evident at the top of the domain, and the structure of the deeper layers is dominated by the strong low-entropy downdrafts that originate from the surface layers. In practice, the maximum effective Reynolds number we can achieve in simulations with a constant coefficient of kinematic viscosity is less than that of simulations that hold the coefficient of dynamic viscosity constant. This limitation is due to numerical noise that develops when the size of evolving magnetic features becomes of order the grid spacing.

We note that although our calculations are not strictly compressible (the time-derivative term in the continuity equation is of sufficiently high order to be neglected in the anelastic approximation), neither are they incompressible. Density is not assumed constant; our computational domain spans over 5.25 pressure scale heights, and there is a density difference of ~ 20 between the upper and lower boundaries. We define a measure of vertical flow asymmetry as $\xi \equiv V^-/V^+$; here $V^{\pm} \equiv \int_A v^{\pm} \, dA / \int_A g^{\pm} \, dA$, with the definitions $v^- = v$ and $g^- = 1$ if $v \leq 0$ ($v^- = 0$ otherwise), and $v^+ = v$ and $g^+ = 1$ if $v > 0$ ($v^+ = 0$ otherwise). We plot V^+ and V^- in Figure 2 along each horizontal slice as a function of height for our initial states (the constant-μ and constant-ν nonrotating-model convection zones). Figure 2 shows that we successfully reproduce the asymmetric flow patterns characteristic of fully compressible
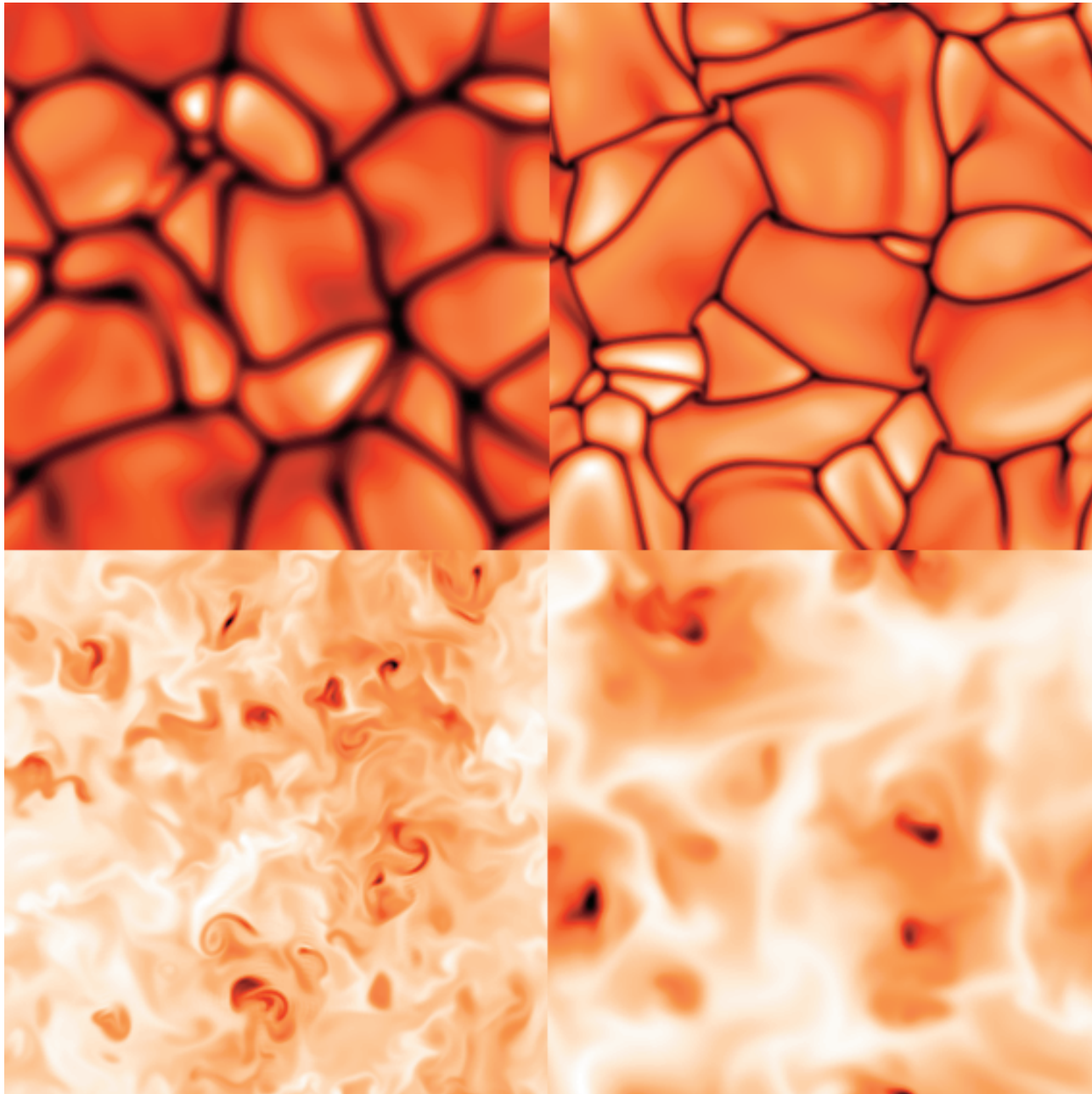
Fig. 1.—Entropy perturbations of two of the thermally relaxed field-free convective states (runs I1 and I2) along horizontal slices toward the top of the computational domain (*top*) and near the base of the box (*bottom*). *Left*, Model convection zone where μ is held constant; *right*, model convection zone where ν is held constant. Darker colors indicate cooler plasma.

three-dimensional simulations of stratified convection (cf. Fig. 5 in Stein & Nordlund 1998).

3.1. *The Decay of Weak Flux Ropes*

We begin by analyzing a set of simulations in which a "neutrally buoyant," untwisted magnetic flux tube is inserted at the center of each of the nonrotating-model convection zones. This is achieved by adding an initial entropy perturbation along the entirety of the tube sufficient to inhibit its natural tendency to rise. Admittedly, this is an unphysical configuration; however, it allows us to isolate the effect of convective turbulence from that of magnetic buoyancy. Figure 3 shows how convection can affect the initial evolution of a neutrally buoyant, untwisted horizontal flux rope. The image is a volume

rendering of $|\boldsymbol{B}|$ for run H1 at $t = 4$ (in units of H_r/v_c). In this simulation, the initial axial field strength of the tube is set to $B_0 = B_{\mathrm{eq}}$. This value is a factor of ~ 3 below the critical value $B_c = \left(H_p/a\right)^{1/2} B_{\mathrm{eq}}$ of Paper I (here H_p denotes the local pressure scale height), above which the magnetic buoyancy force of the tube overcomes the hydrodynamic force of convective flows, and the tube retains its cohesion. Figure 3 demonstrates how a flux rope can be rapidly distorted by convective turbulence and can evolve into a relatively complex magnetic configuration.

To gain a quantitative understanding of the tube's cross-sectional structure, we define the average height of the flux rope at each time step to be the horizontal average of the two-dimensional magnetic field-weighted first moments of position
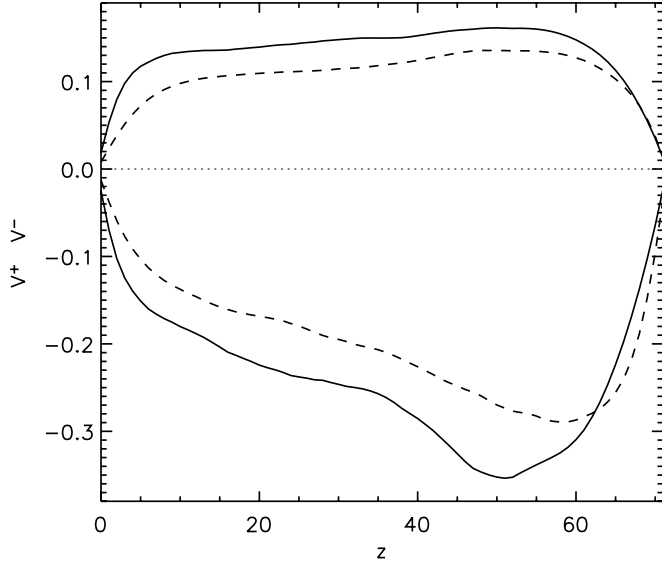
FIG. 2.—Asymmetric flow pattern of three-dimensional convection for both the constant-ν (*dashed line*) and constant-μ (*solid line*) nonrotating initial states (runs I1 and I2, respectively). Shown are the horizontally averaged magnitudes of upflows and downflows V^+ and V^- (as described in the text) as a function of depth. Note that each model convection zone has impenetrable upper and lower boundaries. Velocities are expressed in dimensionless units (see text for details), and z is given in terms of grid zones.

along each vertical slice through the Cartesian domain (of size $L_x \times L_y \times L_z$),

$$\langle z \rangle = \frac{1}{L_x} \int_0^{L_x} \bar{z}_x \, dx, \qquad (11)$$

where

$$\bar{z}_x = \frac{1}{\phi_x} \int_0^{L_z} \int_0^{L_y} z|\boldsymbol{B}(x, y, z)|dy \, dz, \qquad (12)$$

$$\phi_x = \int_0^{L_z} \int_0^{L_y} |\boldsymbol{B}(x, y, z)|dy \, dz. \qquad (13)$$

We further define a field-weighted second moment to describe the horizontally averaged spread of the flux rope,

$$\langle \sigma^2 \rangle = \frac{1}{L_x} \int_0^{L_x} \sigma_x^2 \, dx, \qquad (14)$$

where

$$\sigma_x^2 = \frac{1}{\phi_x} \int_0^{L_z} \int_0^{L_y} \left[(y - \bar{y}_x)^2 + (z - \bar{z}_x)^2 \right] |\boldsymbol{B}(x, y, z)|dy \, dz, \qquad (15)$$

$$\bar{y}_x = \frac{1}{\phi_x} \int_0^{L_z} \int_0^{L_y} y |\boldsymbol{B}(x, y, z)| \, dy \, dz. \qquad (16)$$

Although the temporal evolution of the tube's magnetic field along any given vertical slice can differ greatly from one region of the model convection zone to another, we find that the spatially averaged quantities $\langle \sigma^2 \rangle$ and $\langle z \rangle$ evolve in a much simpler manner. The large-scale convective flows on average advect flux away from the central axis of the tube. Although the interaction of these flows with the magnetic flux tube is not

(strictly speaking) a diffusive process, we can successfully describe the evolution of the spatially averaged quantities of run H1 using a simple two-dimensional eddy-diffusivity treatment, even though the spatial scale of the convective eddies exceeds the cross-sectional diameter of the tube. To demonstrate, we consider the diffusion equation

$$\frac{\partial f}{\partial t} - \nabla \cdot (D\nabla) f = 0. \qquad (17)$$

Here f is a scalar quantity, and D is the coefficient of eddy diffusivity, which we take to be roughly proportional to the product of the volume-averaged rms fluid velocity and convective cell size.

If we assume that the magnetic field acts as a passive scalar with a horizontally averaged evolution that can be described by a two-dimensional diffusion equation where $f \equiv \langle B \rangle_x$ and we further assume that near the center of the domain the coefficient of eddy-diffusivity is constant, then we can analytically solve equation (17) given the initial axisymmetric Gaussian distribution of equation (9) along a vertical slice:

$$f(r, t) = \frac{B_0 a^2}{\sigma^2(t)} e^{-r^2/\sigma^2(t)}, \qquad (18)$$

where $r^2 = y^2 + z^2$ and

$$\sigma^2(t) = a^2 + 4Dt. \qquad (19)$$

Given an estimate for D, we can compare the average spread of the simulated flux rope at each time step (eq. [14]) with the result obtained via the diffusion equation (eq. [19]). Of course, our model convection zone exhibits the asymmetric flow patterns and depth-dependent characteristic-length scales expected in a stratified medium; thus, any eddy-diffusion coefficient derived from a detailed analysis of the convective flow patterns will almost certainly be nonisotropic and depth dependent. Even so, we proceed on the assumption that D is isotropic and spatially constant along the length of the flux rope and obtain a rough estimate for D by using the simulated data to calculate the correlation length L of the vertical flows and the rms velocities V at the tube's initial position.

For run H1, we find that $L = 0.814 H_r$ and $V = 0.363 v_c$, which yield the estimate $D = (\Gamma/3)VL = 0.057$ (in normalized units) for a dimensionless scale factor Γ of 0.58. With D specified, we compare the time evolution of $\langle \sigma^2 \rangle$ measured directly from the MHD simulation with that obtained via the solution of the eddy-diffusion equation and plot the result in Figure 4. It is important to note that the magnetic diffusion time in our simulations (set by the choice of magnetic Reynolds number, R_m) greatly exceeds the characteristic time-scale of the simulations $t_c = H_r/v_c$; thus, we are simulating the effects of large-scale eddies at convective turnover timescales rather than the effects of magnetic diffusion at long diffusive timescales. To demonstrate that the effects of magnetic and thermal diffusion are not dominant players in the redistribution of flux by the convective eddies of the simulation, Figure 4 also shows the time evolution of the spread of the same, initially neutrally buoyant flux rope placed in a nonconvecting envelope.

Although the magnetic field of run H1 quickly evolves into the complex structure shown in Figure 3, we find that a relatively simple model can successfully characterize the average global properties of this particular flux rope. For runs for which $B_0 > B_{eq}$, this description breaks down since the magnetic field
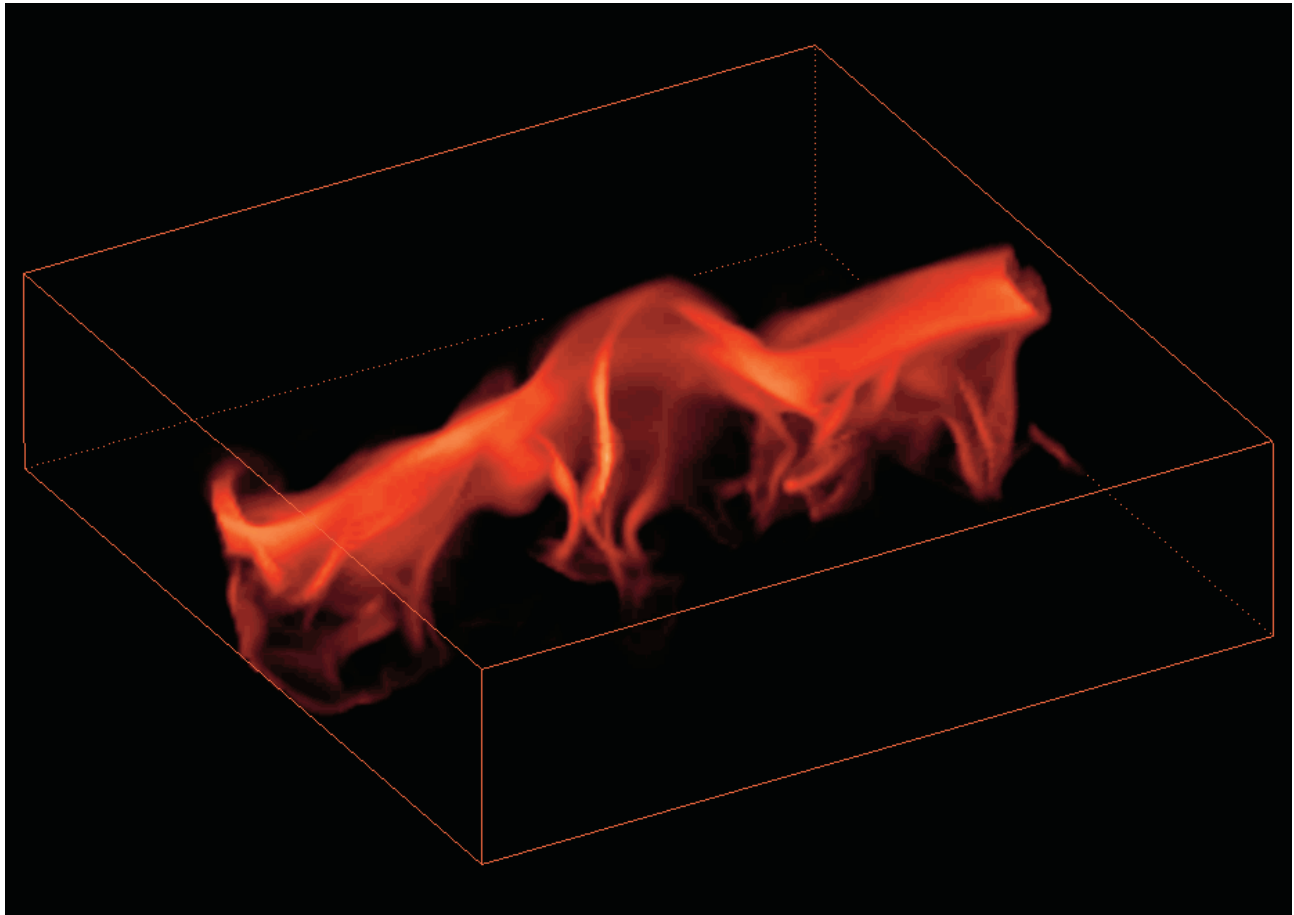
Fig. 3.—Effect of convective turbulence on the untwisted, "neutrally buoyant" flux tube of run H1. The tube was initially positioned at the center of the domain and had an axial field strength of $B_0 = B_{eq}$. This figure is a volume rendering of $|\mathbf{B}|$ at $t = 4.0$ (in normalized units).
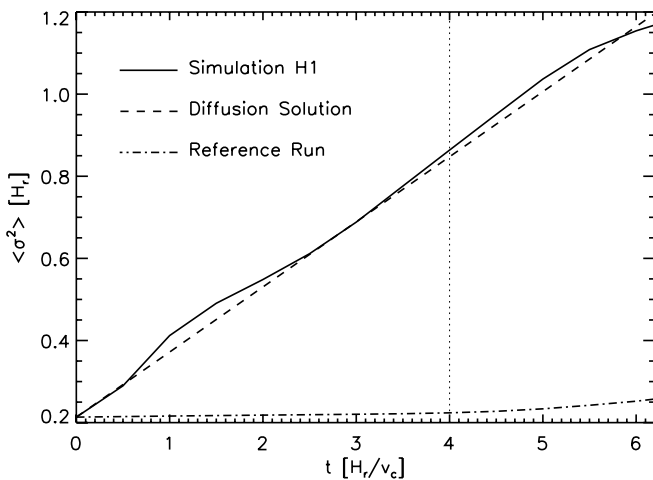

Fig. 4.—Comparison of the horizontally averaged spread of the initially untwisted magnetic flux tube of run H1 data with an estimate obtained by analytically solving the two-dimensional eddy-diffusion equation in the fluid limit with $D = (\Gamma/3)VL = 0.057$ and $\Gamma = 0.58$ (in normalized units; see text for details). The vertical dotted line represents the time that corresponds to the image of Fig. 3. Also shown for comparison is the evolution of the spread of a reference run in which the same neutrally buoyant flux tube is placed in a nonconvecting background. The small increase in the spread after $t = 4.5$ reflects the tube's growth in buoyancy due to thermal diffusion.

strength of the structures is sufficient to disrupt the convective flow pattern. Of course, this treatment cannot describe the details of the magnetic structure—for example, the stretching and amplification of the field along the cool narrow downdrafts or the local asymmetries between fields entrained in horizontal and vertical flows—nor can it predict the evolution or equilibrium distribution of the horizontally averaged field when D is strongly depth dependent, since the characteristic size of the large-scale convective eddies exceeds the size of a typical magnetic structure.

3.2. Turbulent Pumping

There are several distinct timescales relevant to our study of the net transport and distribution of magnetic flux in a turbulent model convection zone. The first is the interval $0 < t \lesssim 5t_c$ (recall that $t_c = H_r/v_c$ is the convective timescale), the characteristic interval over which convective flows redistribute the magnetic field of a weak flux tube or layer vertically through the computational domain. The second is the time interval between $\sim 5t_c$ and $\sim 50t_c$, a transitional period during which the field evolves to a steady state distribution. The third time frame of interest begins after $t \sim 50t_c$ and extends out to the final time step. Over this final interval we can determine the asymptotic behavior of the system. We begin our discussion with an analysis of the first time interval of interest: the duration of the initial magnetic structure.

We consider a set of simulations for which neutrally buoyant, relatively weak untwisted magnetic flux tubes
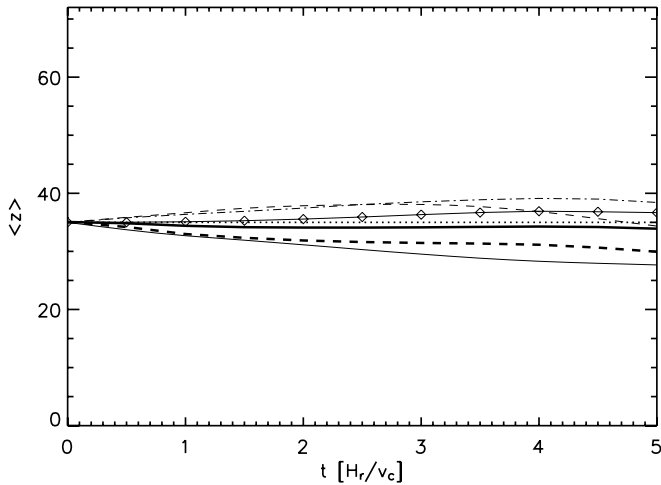
FIG. 5.—Average height $\langle z \rangle$ (in zones) of the magnetic field distribution as a function of time for a subset of the simulations listed in Table 2 for which "neutrally buoyant" flux tubes (*thin lines*) and flux layers (*thick lines*) are positioned at the center of the computational domain. Shown are runs H4 (*thin dashed line*), H5 (*thin solid line*), H6 (*thick dashed line*), and H7 (*thick solid line*). The evolution of $\langle z \rangle$ for the flux tube of Fig. 3 (run H1) is represented by the thin dot-dashed line, and the evolution of $\langle z \rangle$ for reference run R1 is represented by the thin solid line with the overlaid symbols. The horizontal dotted line denotes the initial height of the magnetic structures.

($B_0 = 0.1 B_{eq}$ and $q = 0$ in eqs. [8]–[10]) are centered at $(y, z) = (L_y/2, L_z/2)$ in both constant-μ and constant-ν turbulent model convection zones. The simulations are allowed to progress until a significant amount of magnetic flux has interacted with the closed upper and lower boundaries. For each run, we calculate the average field-weighted position $\langle z \rangle$ (as defined by eq. [11]) at each time step and plot the results in Figure 5. For reference, we also show the evolution of $\langle z \rangle$ for an initially untwisted, neutrally buoyant tube embedded in a *non*convecting, adiabatically stratified domain (run R1 of Table 1). The slight drift of $\langle z \rangle$ in this case gauges the effect of numerical perturbations on the initial state (in unstable equilibrium) and gives a measure of the growth in buoyancy due to thermal diffusion. Figure 5 shows that on average $\langle z \rangle$ tends to remain at or near the center of the box over the lifetime of a magnetic flux tube. The spread evident in the flux tube runs of Figure 5 (*thin lines*) is a result of the sensitivity of the tube's evolution to its initial placement (e.g., whether it is inserted into the domain in the proximity of a strong downflow).

Since the initial evolution of a magnetic flux tube is sensitive to its position relative to strong downdrafts, we follow Tobias et al. (2001) and Dorch & Nordlund (2001) and initiate additional simulations with neutrally buoyant horizontal magnetic layers (Fig. 5, *thick lines*) and with a horizontal magnetic field that permeates the entirety of the computational domain. We focus our attention on four runs in particular: LT1–LT4 (see Table 3). As in run H1 of Figure 3, run LT1 describes the evolution of a neutrally buoyant, horizontal, untwisted flux tube of axial field strength $B_0 = B_{eq}$ (in this particular run, the initial flux tube was positioned two zones below $L_z/2$), while run LT2 describes the evolution of a neutrally buoyant horizontal field of $B_0 = 5 \times 10^{-2} B_{eq}$ initially confined to a 10 zone–thick layer positioned at the same height. In runs LT3 and LT4, the entire domain is initially threaded with a constant B_0 of $10^{-2} B_{eq}$ and $10^{-4} B_{eq}$, respectively (the latter being firmly in the kinematic regime throughout the domain, even later in the run when magnetic fields become

locally concentrated in downdrafts). Each of these simulations was allowed to proceed over a sufficiently long time interval that meaningful temporal averages of steady state flux distributions could be calculated. Runs LT1 and LT2 concluded at $t = 200 H_r/v_c$ and $t = 100 H_r/v_c$, respectively, and runs LT3 and LT4 progressed through $t = 350 H_r/v_c$. We note that the diffusion timescale (as specified by the magnetic Reynolds numbers of Table 3) far exceeds the total length of each run.

Figure 6 shows a volume rendering of $|\boldsymbol{B}|$ for runs LT1 (Fig. 6, *left*) and LT2 (Fig. 6, *right*) and gives a qualitative picture of the evolution of the magnetic structures. The right-hand coordinate system is displayed such that z increases vertically and y increases from right to left (i.e., the reader faces the boundary at $x = 0$); thus, the horizontal tube of run LT1 is essentially viewed along its axis. It is apparent in Figure 6 that by $t = 10$ convective flows have redistributed the magnetic field to the point where the initial structures are no longer recognizable and a number of new, distinct magnetic structures have formed (see, e.g., the new flux tube at $t = 10$ in Fig. 6, *right*). It is possible to infer from the volume renderings that a significant amount of the field of run LT1 is initially redistributed to the upper half of the domain (since the narrow tube is pinned down by downflows at only two locations), while the strongest magnetic fields of run LT2 reside in the lower half of the domain. This qualitative interpretation is consistent with the evolution of $\langle z \rangle$ for runs H4 (*thin dashed line*) and H6 shown in Figure 5 (*thick dashed line*).

It is important to recognize that $\langle z \rangle$ is a measure of the average distribution of a nonconserved quantity $|\boldsymbol{B}|$ and is sensitive to the effects of field amplification and the local dynamo. To obtain a more direct picture of the distribution of magnetic *flux* (a conserved quantity) in runs LT1 and LT2, we show the initial evolution of the signed flux threading a vertical slice (a y-z plane positioned at $x = 109$) through each domain in Figure 7. Light shades correspond to positive-signed flux (the component of the magnetic field in the $\hat{x}$-direction points toward the reader), and dark shades correspond to negative-signed flux (the $\hat{x}$-component of the field points away from the reader and into the page). Since the upper and lower boundaries are impenetrable and the field is divergence-free, the total amount of flux threading any given vertical slice remains constant in time.

For run LT1 (Fig. 7, *left*) we can obtain a qualitative picture of the transport of magnetic flux along this vertical slice. Since this portion of the tube is not pinned down by a strong downflow during this time period (the flux is instead entrained in broad, slower moving upflows), there is an initial, net transport of magnetic flux into the upper half of the domain. The situation is not quite as clear for run LT2 (Fig. 7, *right*); however, we can clearly see that by $t = 10$ a strong, oppositely directed field is being generated in and around downdrafts in the lower half of the domain, and thus, a greater proportion of unsigned flux is concentrated in this region.

We now calculate the average amount of signed flux threading vertical slices through the lower half of the domain,

$$\langle \Phi_l \rangle = \frac{1}{L_x} \int_0^{L_x} dx \left[\int_0^{L_y} dy \int_0^{z_0} dz\, B_x(x, y, z, t) \right]. \quad (20)$$

Here $z_0 = L_z/2$, and we note that $\langle \Phi_l \rangle$ is time dependent. The total amount of flux threading any given vertical slice remains constant; thus, any increase in $\langle \Phi_l \rangle$ is accompanied by a
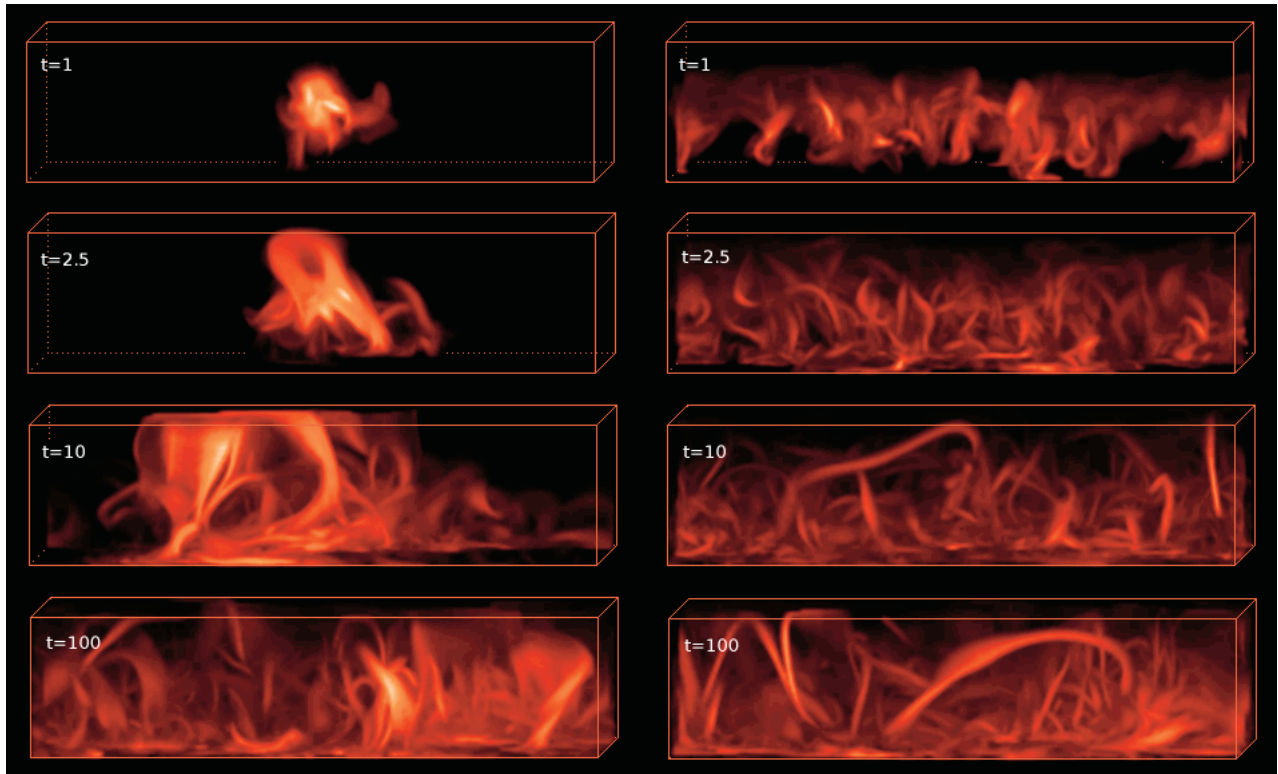
Fig. 6.—Volume renderings of $|\boldsymbol{B}|$ for four characteristic times during runs LT1 (*left*) and LT2 (*right*). The coordinate system is displayed such that z increases vertically, y increases from right to left, and x increases into the page.

decrease in the average amount of signed flux residing in the upper half of the simulation domain. Of particular interest is the initial evolution of $\langle\Phi_l\rangle/\langle\Phi\rangle$ (the total flux $\langle\Phi\rangle$ is defined by eq. [20] with $z_0 = L_z$) for runs LT3 and LT4, simulations that are initiated with a domain-filling magnetic field of the form $\boldsymbol{B} = B_0\hat{\boldsymbol{x}}$. Figure 8 (*top*) shows $\langle\Phi_l\rangle/\langle\Phi\rangle$, along with the

corresponding evolution of the unsigned field-weighted moment $\langle z\rangle$ (Fig. 8, *bottom*) for each run. Figure 8 (*top*) shows that in the interval $0 < t \lesssim 4t_c$, there is no net transport of signed flux toward the base of the computational domain despite the presence of flow asymmetries characteristic of stratified convection (see Fig. 2).
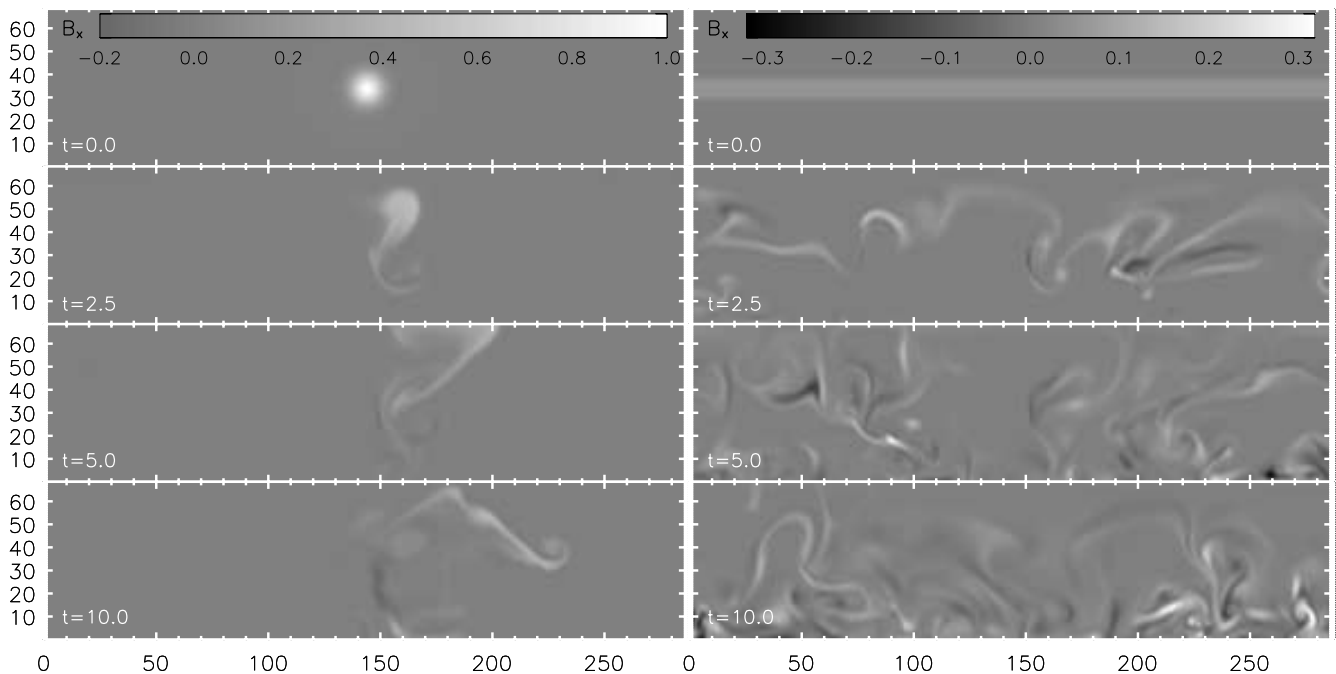
Fig. 7.—B_x along a vertical y-z slice positioned at $x = 109$ (the total number of grid cells in the $\boldsymbol{x}$-direction is 288). B_x is displayed in normalized units (see text for details). *Left,* LT1; *right,* LT2.
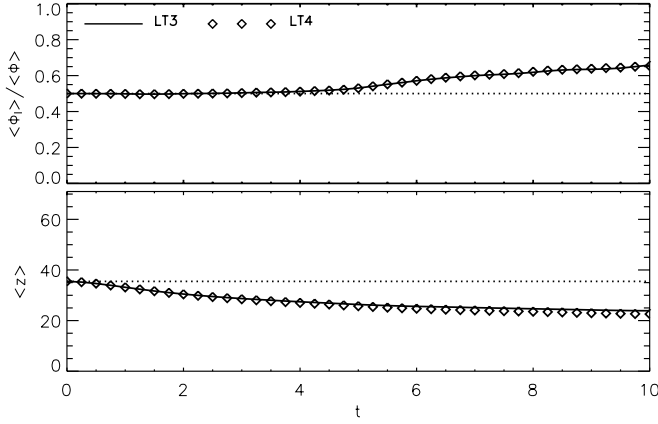
FIG. 8.—*Top*, Normalized amount of signed flux as a function of time that resides in the lower half of the Cartesian domain for runs LT3 and LT4; *bottom*, height of the unsigned field distribution for each of the runs. Time is displayed in units of H_r/v_c.
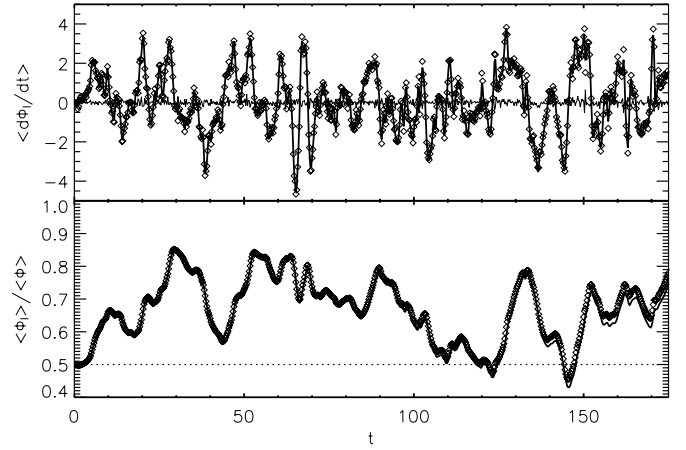

FIG. 9.—*Top*, Horizontally averaged time rate of change of magnetic flux entering into the lower half of the domain of run LT3 at a given time (*thick solid line*), the ideal contribution calculated via eq. [26] (*symbols*), and the resistive contribution (*thin solid line*); *bottom*, normalized signed flux residing in the lower half of the domain as a function of time (*solid line*) and the contribution due to a net electric field in the *y*-direction along a plane at $z = L_z/2$ (*symbols*). Time is displayed in units of H_r/v_c.

To obtain a qualitative understanding of this result, we neglect the effects of Lorentz forces and magnetic diffusion and consider the ideal MHD induction equation,

$$\frac{\partial \boldsymbol{B}}{\partial t} = \nabla \times (\boldsymbol{v} \times \boldsymbol{B}). \qquad (21)$$

Applying Stokes' theorem to equation (21) gives

$$\frac{d}{dt} \int_A \boldsymbol{B} \cdot d\boldsymbol{A} = \oint \boldsymbol{v} \times \boldsymbol{B} \cdot d\boldsymbol{l}. \qquad (22)$$

Since we are interested in how magnetic flux threading vertical slices through the volume is redistributed (on average), we evaluate the line integral of equation (22) for a closed circuit encompassing the lower half of a single *y-z* slice through our Cartesian domain. Since our domain is periodic in the horizontal directions, and since the lower boundary of the computational domain is assumed impenetrable (the vertical components of $\boldsymbol{v}$ and $\boldsymbol{B}$ are antisymmetric across the lower boundary and thus vanish at $z = 0$), the only contribution to the line integral is at $z = L_z/2$. Then the time rate of change of magnetic flux in the lower half of the vertical slice (at a given instant in time) is simply

$$\frac{d\Phi_l}{dt} = \int_0^{L_y} (v_x B_z - v_z B_x)_{z = L_z/2} \, dy. \qquad (23)$$

Initially, the imposed magnetic field is of the form $\boldsymbol{B} = B_0\hat{\boldsymbol{x}}$ (B_0 is assumed constant). Thus, the only way the total amount of magnetic flux through any *y-z* slice above or below the horizontal layer of height $z_0 = L_z/2$ can change is by the interaction of vertical flows with the initially horizontal flux layer. Then the average change in flux in the lower half of the volume can be initially expressed as

$$\frac{d}{dt} \langle \Phi_l \rangle = -\frac{B_0}{L_x} \int_0^{L_x} dx \left(\int_0^{L_y} dy \, [v_z]_{z = z_0} \right). \qquad (24)$$

In our implementation of anelastic MHD (ANMHD), it is assumed that the horizontal average of v_z is zero at each height

in the atmosphere (i.e., there is no bulk flow or net vertical pulsation in the plane-parallel domain); thus,

$$\frac{d}{dt} \langle \Phi_l \rangle = 0, \qquad (25)$$

and we should expect no *initial* systematic tendency for horizontal magnetic flux layers to be preferentially transported in one vertical direction over the other solely as a result of the presence of an asymmetric vertical flow field.

To extend our treatment beyond the initial stages of the simulations, we take the horizontal average of equation (23),

$$\frac{d}{dt} \langle \Phi_l \rangle = \frac{1}{L_x} \int_0^{L_y} \langle v_x B_z \rangle_{z_0} - \langle v_z B_x \rangle_{z_0} \, dy; \qquad (26)$$

here we introduce the notation $\langle f \rangle_{z_0} \equiv \int_0^{L_x} [f]_{z=z_0} \, dx$ (note that $\langle f \rangle_{z_0}$ is a function of y alone). The first term of the integrand represents the average increase or decrease of magnetic flux in the lower half of the domain due to flows in the *x*-direction that tilt vertical field lines that thread the $z = L_z/2$ plane, and the second term represents the average transport of magnetic flux resulting from asymmetric vertical flows acting on the horizontal component of the magnetic field. In the MHD approximation, the electric field is expressed as $\boldsymbol{E} = -(\boldsymbol{v} \times \boldsymbol{B})/c$. Thus, equation (26) simply states that there is a net transport of magnetic flux into the lower (upper) half of the domain in our simulations if and only if there is a net positive (negative) component of the electric field in the $\hat{\boldsymbol{y}}$-direction along a horizontal plane positioned at $z_0 = L_z/2$.

Integrating equation (26) with respect to time yields an expression for the evolution of $\langle \Phi_l \rangle$,

$$\langle \Phi_l(t) \rangle = \langle \Phi_l(0) \rangle + \int_0^t \int_0^{L_y} \langle v_x B_z - v_z B_x \rangle_{z_0} \, dy \, dt'. \qquad (27)$$

Note that for runs LT3 and LT4, $\langle \Phi_l(0) \rangle = B_0 L_y L_z/2$. Figure 9 (*bottom*) compares the normalized signed flux residing in the lower half of the domain of run LT3 obtained directly from the volume data sets via equation (20) with the ideal contribution due to the presence of a net electric field in the $\hat{\boldsymbol{y}}$-direction
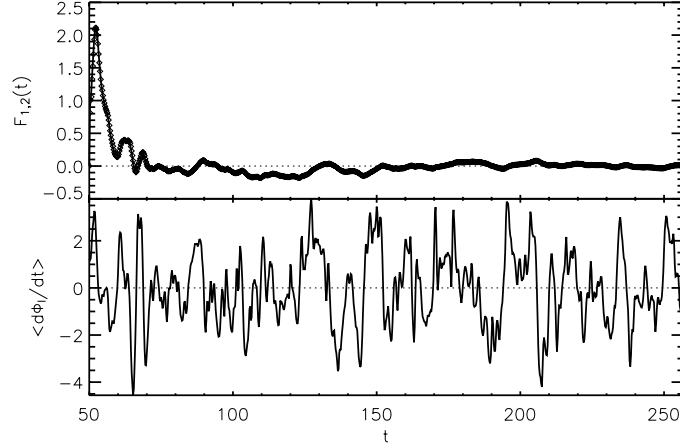
Fig. 10.—*Top*, $F_1(t)$ (*solid line*) and $F_2(t)$ (*symbols*) for run LT3 (see text for the definitions of these quantities); *bottom*, $\langle d\Phi_l/dt\rangle$ for the interval between $t = 50$ and 257. Again, the time is displayed in normalized units of H_r/v_c.

along the horizontal plane positioned at $z = L_z/2$ (using eq. [27]). The slight difference in the two curves (noticeable after $t \sim 150$) reflects the cumulative effect of magnetic diffusion, a quantity not included in the derivation of equation (27) for the sake of simplicity. Figure 9 (*top*) compares the ideal and resistive contributions (the former calculated via eq. [26]) with the horizontally averaged time rate of change of magnetic flux in the lower half of the domain (obtained by evaluating the normalized time derivative of eq. [20]).

We now focus on the long-term asymptotic behavior of run LT3 and consider the time average of equation (26) over increasing intervals in the period between $t_0 = 50$ (after the vertical magnetic field has concentrated in downdrafts and intergranular lanes) and t, $F_1(t) \equiv 1/\Delta t \int_{t_0}^{t} \int_{0}^{L_y} \langle E_y\rangle_{z_0} \, dy \, dt'$. Again, $z_0 \equiv L_z/2$ and $\Delta t \equiv t - t_0$ for $t > t_0$. We plot this quantity in Figure 10 (*top*) over the interval $t_0 \leq t \lesssim 250$ and compare it with $F_2(t) \equiv 1/\Delta t \int_{t_0}^{t} f(t') \, dt'$, for which we obtain $f(t) \equiv \langle d\Phi_l/dt\rangle$ (Fig. 10, *bottom*) through a direct evaluation of the simulated data sets via equation (20). It is clear that for a sufficiently long time interval, $1/\Delta t \int_{t_0}^{t} \int_{0}^{L_y} \langle E_y\rangle_{z_0} \, dy \, dt' \to 0$; thus, over time in run LT3, there is no net transport of magnetic flux into (or out of) the lower half of the domain after $t = t_0$.

Yet, Figure 11 shows that there is a relatively short period of time after the initial stage of the run ($0 < t < 5$; see Fig. 8) but before t_0 during which there is a modest net transport of magnetic flux into the lower half of the domain, where it remains (on average) for the rest of the simulation. This is most easily seen in Figure 11 (*bottom*), where we plot at each time step a new quantity, $\langle \zeta \rangle = 1/L_x \int_{0}^{L_x} \overline{\zeta}_x \, dx$ (*solid white line*), that better characterizes the evolution of the average distribution of signed flux along vertical slices throughout the domain. Here $\overline{\zeta}_x$ is the analog of equation (12),

$$\overline{\zeta}_x = \frac{1}{\psi_x} \int_{0}^{L_z} \int_{0}^{L_y} z B_x(x, y, z) \, dy \, dz, \qquad (28)$$

and $\psi_x \equiv \int_{0}^{L_z} \int_{0}^{L_y} B_x(x, y, z) \, dy \, dz$. Also shown in Figure 11 (*bottom*) is the evolution of $\langle z \rangle$ (*dashed white line*) and the
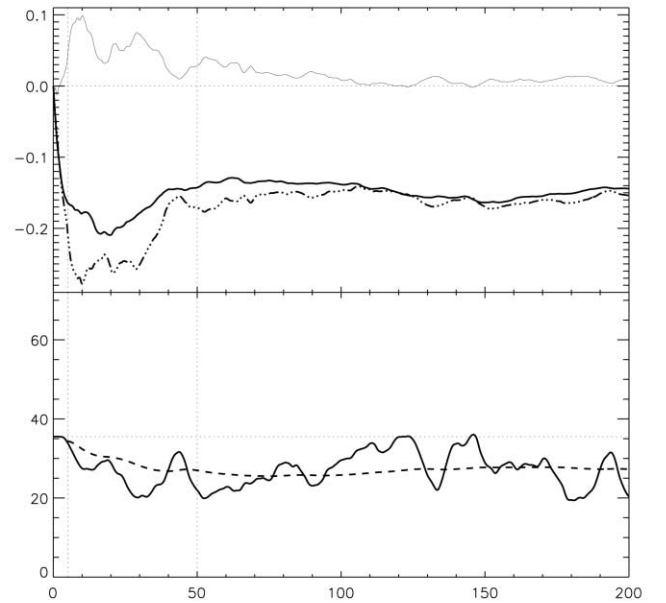

Fig. 11.—*Top*: Normalized average amount of magnetic flux that resides in the lower (*solid white line*) and upper (*solid black line*) halves of the domain. The gray dashed line denotes half the total flux, $\int_V B_x \, dV$, a conserved quantity. The background gray-scale image corresponds to $\int_A B_x \, dV$ ($A = L_x L_y$) along each horizontal slice; the lighter the shade, the stronger the field at that height. *Bottom*: $\langle \zeta \rangle$ at each time step (*solid white line*), $\langle z \rangle$ (*dashed white line*), and the ρ_0-weighted moment of the background stratification (*black line*). The horizontal dotted line denotes the midplane of the domain. The shading corresponds to $\int_A |\boldsymbol{B}| dA$ for each horizontal layer (the *y*-axis in the background image corresponds to the vertical extent of the domain); lighter colors correspond to large positive values. Time is displayed in units of H_r/v_c.

Fig. 12.—*Top*, $\psi_1 = 1/t \int_{0}^{t} \int_{0}^{L_y} \langle v_x B_z\rangle_{z_0} \, dy \, dt'$ (*thick solid line*), $\psi_2 = 1/t \int_{0}^{t} \int_{0}^{L_y} \langle v_z B_x\rangle_{z_0} \, dy \, dt'$ (*dot-dashed line*), and $F_1(t) = 1/t \int_{0}^{t} \int_{0}^{L_y} \langle E_y\rangle_{z_0} \, dy \, dt'$ (*thin solid line*), the average change of magnetic flux across the domain's midplane for run LT3; *bottom*, evolution of $\langle \zeta \rangle$ in grid units (*solid line*) and its associated time average, $\psi_3 = 1/t \int_{0}^{t} \langle \zeta \rangle dt'$ (*dashed line*) for run LT3. See text for details. The vertical dotted lines bound the interval $5 < t < 50$, and t is given in units of H_r/v_c.
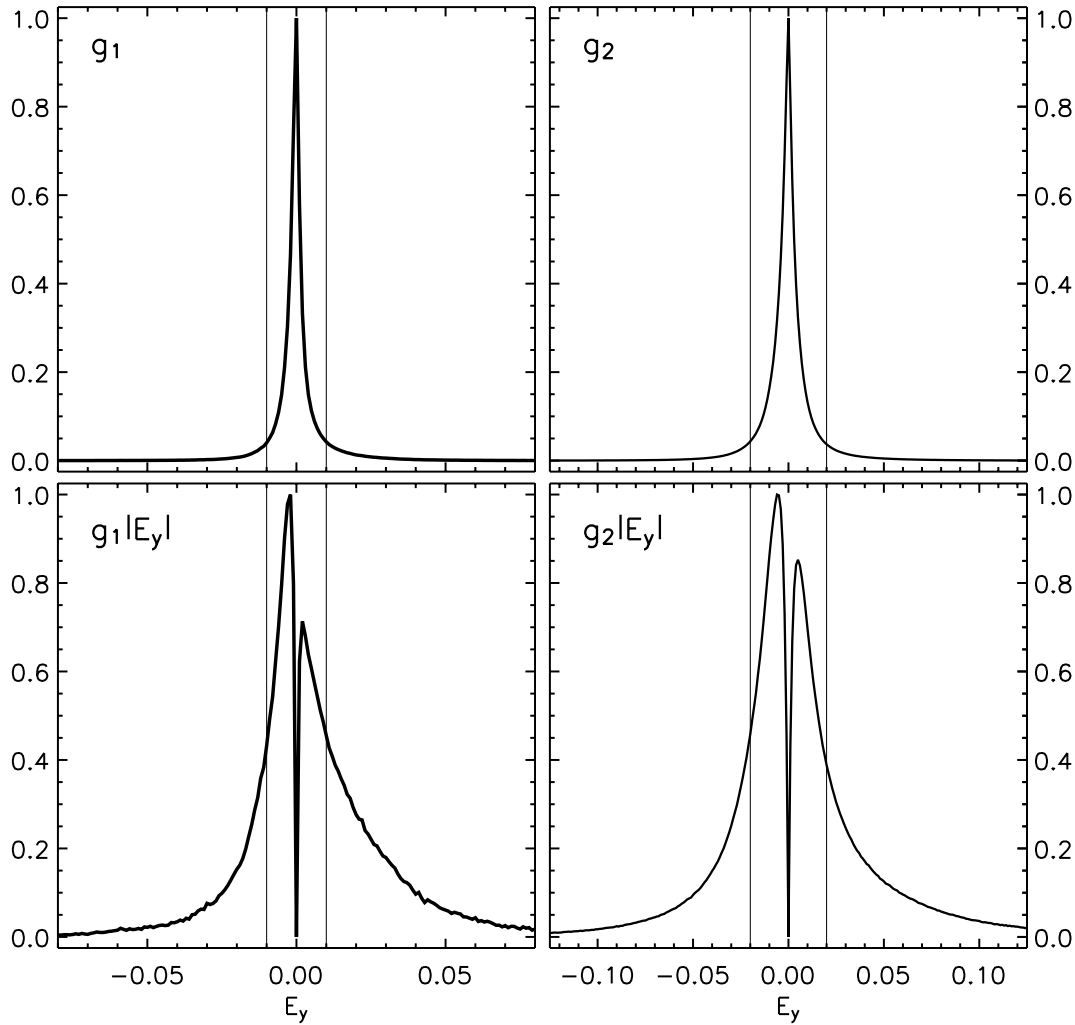
FIG. 13.—*Top*, Average normalized distribution functions g_1 and g_2 for the $\hat{y}$-component of the electric field along the midplane during the time intervals $5 < t < 20$, and $50 < t < 250$, respectively (time is in units of H_r/v_c); *bottom*, $g(E_y)|E_y|$, the contribution per unit dE_y to the integral $\int g(E_y) E_y \, dE_y$ (we show the absolute value here to more easily visualize asymmetries in the above integral).

density-weighted moment of the background stratification, $\langle z_\rho \rangle = 1/M \int_V z\rho_0 \, dV$ (where $M = \int_V \rho_0 \, dV$; *black line*). Note that on average $\langle z \rangle > \langle z_\rho \rangle$. This reflects the fact that over time B/ρ is not constant (as would be expected if the magnetic field acted as a passive scalar and was mixed throughout the domain via a mechanism similar to that described in Miesch et al. 2000); rather, it gradually increases with height through the center of the domain. The upper frame shows the average amount of magnetic flux residing in the lower (*solid white line*) and upper (*solid black line*) halves of the domain ($\langle \Phi_l \rangle$ and $\langle \Phi_u \rangle$, respectively). The latter quantity is shown along with $\langle \Phi_l + \Phi_u \rangle/2$ (*gray dashed line*) to demonstrate that flux is conserved in the simulations and that there is no diffusive flux loss through either vertical boundary. The gray-scale image in Figure 11 (*top*) corresponds to the total amount of $\hat{x}$-directed field along a horizontal plane at each height z, $\phi(z) = \int_0^{L_x} \int_0^{L_y} (B_x)_z \, dx \, dy$; the lightest shades correspond to the largest positive values of ϕ. We display this quantity to get a qualitative feeling for the average distribution of signed flux as a function of height. Similarly, the background image in Figure 11 (*bottom*) corresponds to the total magnitude of the field integrated over each horizontal plane.

We now consider the transition interval $5 < t < 50$ (bounded by the two vertical dotted lines in each frame of Fig. 11),

where there is a slow net transport of flux across the midplane of the domain. In Figure 12 (*top*) we plot the running time averages of each term in the integrand of equation (26), $\psi_1 = 1/t \int_0^t \int_0^{L_y} \langle v_x B_z \rangle_{z_0} \, dy \, dt'$ (*solid line*) and $\psi_2 = 1/t \int_0^t \int_0^{L_y} \langle v_z B_x \rangle_{z_0} \, dy \, dt'$ (*dot-dashed line*). The thin solid line represents the average time rate of change of flux in the lower half of the domain, $F_1(t) = 1/t \int_0^t \int_0^{L_y} \langle E_y \rangle_{z_0} \, dy \, dt'$, the difference of the two previous quantities. Where $\psi_2 < \psi_1$ by a significant margin (e.g., between $t = 5$ and 50), there is a net transport of magnetic flux across the midplane (as is evident in Fig. 11). This result is reinforced in Figure 12 (*bottom*), where we show the evolution of $\langle \zeta \rangle$ (*solid line*) along with its associated running average $\psi_3 = 1/t \int_0^t \langle \zeta \rangle \, dt'$ after $t = 5$ (*dashed line*). We note that when $t < 5$ there is little net transport of flux; thus, $\psi_1 \sim \psi_2$ in this interval.

But why does the net transport of magnetic flux occur over this relatively short time interval but at no other time (on average) during the simulations? The answer lies in Figure 13, which shows the average normalized distribution functions g_1 and g_2 for the electric field along the midplane during the time intervals $5t_c < t < 20t_c$, and $50t_c < t < 250t_c$, respectively (the former being the time interval over which the initial flux transport is most pronounced). For each interval we also show the relative contribution of each bin to the integral $\overline{E}_y = \int g|E_y| \, dE_y$
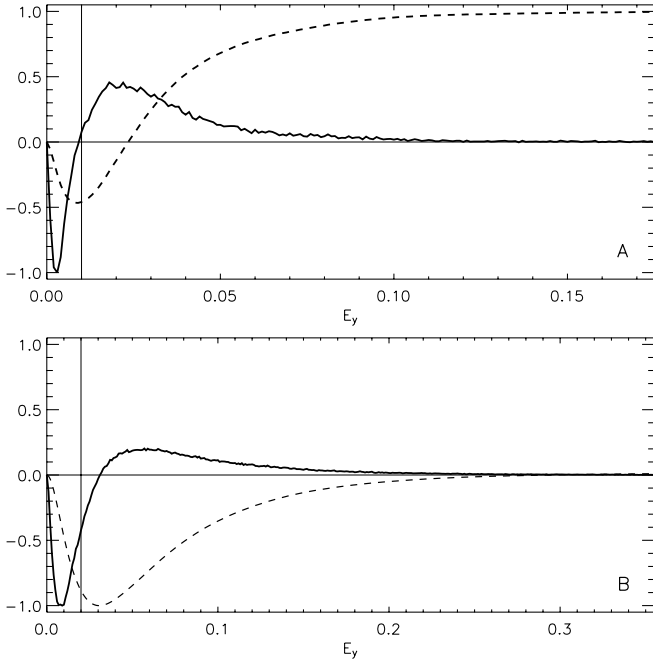
FIG. 14.—(a) $F(E_y) \equiv \int_0^{E_y} (g^+ - g^-) E_y' \, dE_y'$ [where $g^+ \equiv g(E_y')$ and $g^- \equiv g(-E_y')$] for the transition time $0 < t < 20 H_r/v_c$ (dashed line) and its integrand $(g^+ - g^-) E_y'$ (solid line). E_y is expressed in normalized units (see text for details). (b) Same as (a), but for the time interval $50 H_r/v_c < t < 250 H_r/v_c$. Note that if $F(E_y) = 1$ for large E_y, then there is a net downward pumping of flux during the time interval in question (a), and if $F(E_y) = 0$, there is no net flux transport (b).

FIG. 15.—Contribution of vortex flows and vertical magnetic field to the $\hat{y}$-component of the electric field $E_y = v_x B_z - v_z B_x$ along a horizontal plane. See text for details.

(we show the unsigned quantity here to more easily visualize asymmetries in the distributions). Each distribution function g_1 and g_2 is sharply peaked, and we find that a significant contribution to $\overline{E}_y$ comes from the tails of each distribution (each side of the vertical lines in each panel).

During the transition period (Fig. 13, left), it is evident that there is a significant asymmetry in $g_1|E_y|$, as the vertical magnetic field throughout the volume has yet to concentrate and strengthen in regions of high vorticity in and around localized downdrafts. The left tail of the distribution is an important contributor to a net negative E_y along the midplane (the first term in eq. [26], $\langle v_x B_z \rangle_{z_0}$), which, on average after $t \sim 50$, balances the net positive E_y (the second term in eq. [26], $\langle -v_z B_x \rangle_{z_0}$) because of the presence of compressed horizontal fields at the forefront of strong low-entropy downflows.

This initial imbalance is evident in Figure 14a, where we show the quantity $F(E_y) \equiv \int_0^{E_y} (g^+ - g^-) E_y' \, dE_y'$ [where $g^+ \equiv g(E_y')$ and $g^- \equiv g(-E_y')$] (dashed line) for the transition time period along with its integrand $(g^+ - g^-) E_y'$ (solid line). Note that if $F(E_{max}) > 0$ (E_{max} denotes the maximum value of $|E_y|$), then there is a net downward pumping of flux during the time interval in question; similarly, if $F(E_{max}) < 0$ there is a net upward pumping of flux. Figure 14a shows that the imbalance in the wings of the distribution (to the right of the thin vertical line) is clearly responsible for the net downward pumping of flux during the transition interval. In contrast, the contribution to the total component of the electric field in the $\hat{y}$-direction from the tail of the equilibrium distribution ($50 t_c < t < 250 t_c$) is more balanced (see Fig. 14b); thus, there is no longer any net transport of magnetic flux into or out of the lower half of the domain over time [$F(E_y) = 0$ at $E_y = E_{max}$].

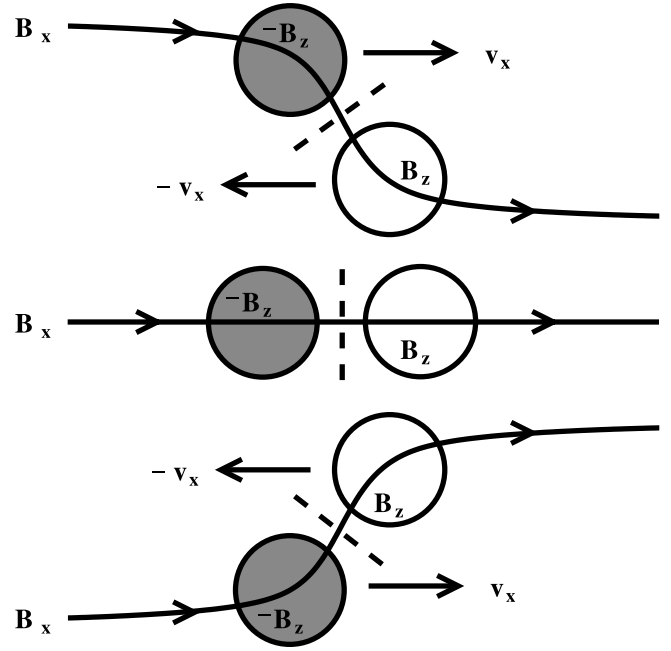To gain physical insight into why the vertical component of the magnetic field associated with vortical flows in down-

drafts provides a component of the electric field that on average balances the contribution due to vertical flows acting on the horizontal component of the magnetic field, consider the following heuristic picture. Imagine we are looking down (in the $-\hat{z}$-direction) on $\hat{x}$-directed magnetic field lines positioned both above and below a horizontal x-y plane (see Fig. 15). Suppose the plane is now pierced by a narrow fast-moving downdraft with negative vorticity (a clockwise-rotating flow). As the downdraft passes through the plane, field lines are entrained and twisted within the flow, and a negative polarity associated with a positive-$\hat{x}$–directed flow forms, while a positive polarity associated with a negative-$\hat{x}$–directed flow forms. That is, in Figure 15, take a horizontal field line, push it into the page (Fig. 15, middle), then rotate it either clockwise (Fig. 15, top) or counterclockwise (Fig. 15, bottom). We see that in each case, the first term of $E_y = v_x B_z - v_z B_x$ is always less than zero (independent of the sign of the vorticity) and counteracts the positive contribution of the second term. In fact, $v_x B_z$ always opposes the contribution of $-v_z B_x$ in this picture, even if we choose a different sign for B_x or v_z (note that in the broad, slower moving upflows, the vertical component of the magnetic field is smaller).

To summarize, we find that the net transport of magnetic flux across the midplane is triggered by a net change in the initial distribution of E_y over that plane. However, once a steady state distribution is reached and the magnetic layer has been expelled from the cell centers into converging downflows and intercellular lanes, the net transport of magnetic flux comes to an end. We note that the amount of magnetic energy (and unsigned flux) can continue to increase as a result of field amplification or the local dynamo; however, these processes do not affect the average distribution of the field and thus do not contribute over time to a net transport of flux either into or out of the lower half of the domain.

If the mere presence of an asymmetric vertical flow field were enough to cause a preferential transport of magnetic flux
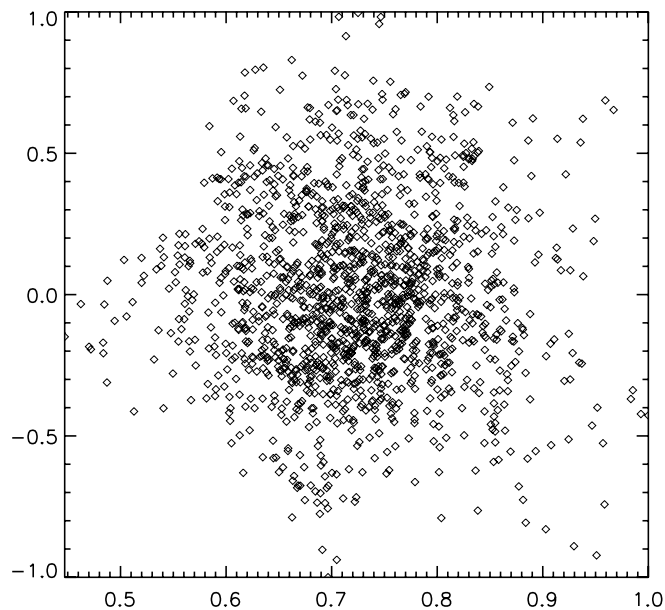
Fig. 16.—Magnitude of the asymmetry ξ at the midplane of run LT3 (*horizontal axis*) vs. $\langle d\Phi_l/dt \rangle$ (*vertical axis*) at each $t = 0.25$ during the interval $0 \leq t \leq 250$ (each quantity is normalized to its maximum value). Time is given in units of H_r/v_c.

to the base of a stratified model convection zone, then the transfer of magnetic flux from the top half to the bottom half of the domain should begin immediately, particularly in the runs LT3 and LT4 when the distribution of the magnetic field is essentially uniform throughout the entire domain. The fact that it does not (see Fig. 8, *top*, in the time interval $0 < t < 4$) indicates that the presence of vertical flow asymmetries alone does not lead to a net downward transport of magnetic flux. We emphasize this point in Figure 16, where we plot the magnitude of the asymmetry ξ at the midplane of run LT3 against $\langle d\Phi_l/dt \rangle$ every $t = 0.25$ during the interval $0 \leq t \leq 250$ (each quantity is normalized to its maximum value). The two quantities are uncorrelated (although one might argue that

for low ξ upward transport predominates); thus, the relative strength or weakness of a vertical flow asymmetry is *not* related to the net downward transport of magnetic flux across a horizontal plane. This is a robust result and applies to all our simulations, regardless of our treatment of viscosity.

It is perhaps not surprising that our simulations lack the highly efficient turbulent pumping mechanism of Tobias et al. (1998, 2001), since we do not include an overshoot layer in our models. Clearly, in the presence of an overshoot layer a magnetic field entrained within strong downdrafts will penetrate into the stable layers below the convection zone and will not be able to reemerge over a typical turnover time. This will surely affect the distribution of the transverse electric field along the midplane of the domain, as flux is trapped in the overshoot layer and cannot be recirculated in broad, slower moving upflows. Thus, in the case of penetrative convection, magnetic flux quickly accumulates in the overshoot layer, leading to a rapid reduction in the amount of flux stored in the convectively unstable layers.

3.3. Buoyant Ω-Loops

We now remove the artificial requirement that initial magnetic flux tubes or layers be neutrally buoyant and turn our attention to simulations of buoyant flux ropes with initial axial field strengths sufficient to allow the flux ropes to retain a tubelike cross section during the entirety of their ascent through the model convection zone. At these field strengths, the flux is no longer passively advected by convective flows; instead, the tube affects the flow pattern, inhibiting even strong downdrafts in regions where the magnetic field is particularly concentrated. We begin by investigating how our two treatments of viscosity (see Fig. 1) affect the evolution of a given flux rope in a nonrotating box.

Figure 17 shows how an initially untwisted, horizontal magnetic flux rope with an axial field strength of $B_0 = 3B_{\rm eq}$ placed at the base of each box has evolved into looplike structures. This choice of B_0 is optimal for this particular experiment, since it is slightly larger than the critical value $B_c \sim (H_p/a)^{1/2} B_{\rm eq}$ of Paper I (here H_p refers to the local pressure
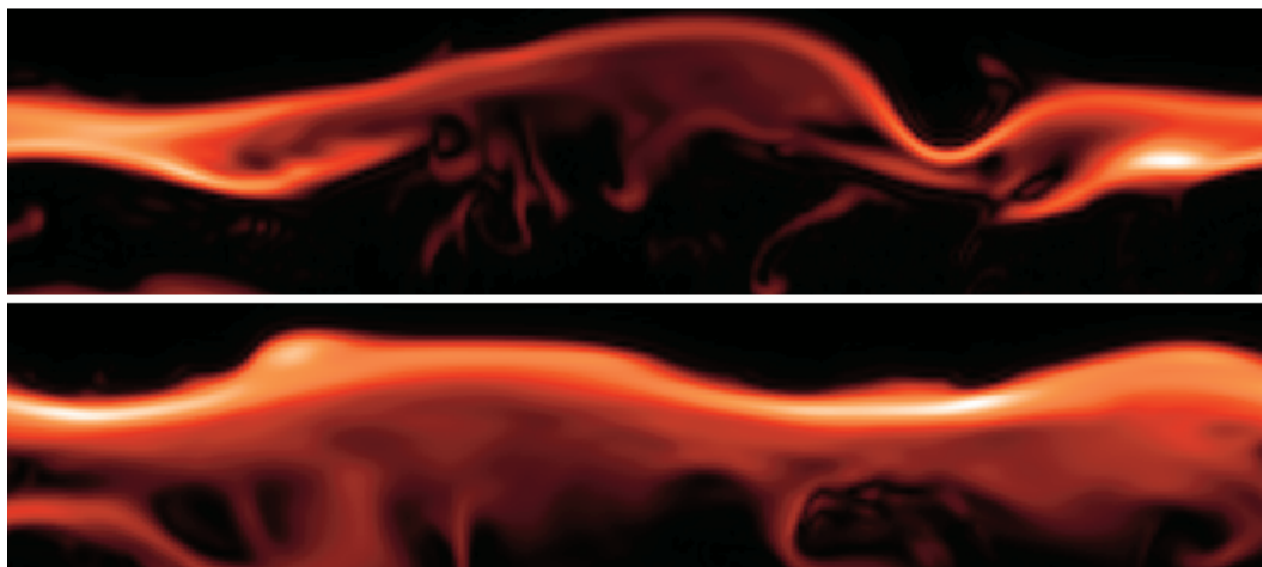

Fig. 17.—$|\mathbf{B}|$ along a vertical slice through the center of the domain for two different untwisted horizontal magnetic flux tube simulations initially positioned near the base of the two distinct model convection zones: one where the kinematic viscosity (ν) is assumed constant with depth (*top*; run B2) and one where the dynamic viscosity ($\mu = \rho_0 \nu$) is assumed constant (*bottom*; run A2). The dips in the flux ropes coincide with areas where there are particularly strong downdrafts.

scale height), above which the magnetic buoyancy force of the tube can overcome the hydrodynamic force of strong downdrafts. Figure 17 (*bottom*) corresponds to run A2, for which the untwisted rope is placed in the model convection zone of constant dynamic viscosity (the state shown in Fig. 1, *left*), and Figure 17 (*top*) corresponds to run B2, for which the same tube is placed in the model convection zone of constant kinematic viscosity. The morphological details of the tubes shown in Figure 17 differ, since the strong downdrafts in each convective starting state are positioned at different locations in the box, and the run for which μ is assumed constant has a higher effective Reynolds number where the tube was initially embedded. However, the general characteristics of loop evolution remain the same in each case; for example, the amount that the tube fragments (as defined in Abbett et al. 2000) during its ascent differs little between runs.

In our simulations, the strength of the axial magnetic field relative to the kinetic energy of strong flows is the dominant factor in determining whether a tube retains its cohesion in the presence of convective turbulence. However, in the absence of convective turbulence, it has been shown that field line twist of an amount greater than that necessary to balance the dynamic pressure gradient due to the buoyant rise of the tube can prevent a flux tube from splitting into counterrotating fragments (see, e.g., Linton et al. 1996; Fan et al. 1998; Emonet & Moreno-Insertis 1998; Abbett et al. 2000). In a similar manner, a twisted flux tube may be able to to maintain its cohesion in a turbulent medium if magnetic tension is able to counteract dynamic forces acting to distort the tube's cross section; that is, if $B_0^2 a/(4\pi L_c^2) + B_0^2 q^2/4\pi a \sim \rho v_c^2/L_c$ (here L_c refers to the correlation length of convective flows). The first term represents the differential restoring force due to the axial component of the magnetic field, and the second term represents the contribution of the azimuthal component (here we have assumed that the length scale of cross-sectional deformation is of order the tube's radius). Then in the absence of twist, the tube retains its cohesion if $\epsilon_B \gtrsim (L_c/a)\epsilon_K$, where $\epsilon_B \equiv B_0^2/8\pi$ and $\epsilon_K \equiv \rho v_c^2/2$ (a result consistent with that of Paper I). If field line twist is present, then the above expression yields an estimate for the amount of twist necessary for a tube with an initial axial field strength of B_0 to resist the destabilizing effects of convective turbulence: $q_c \sim (a/L_c)^{1/2}(v_c/v_A)$ [here $v_A \equiv B_0/(4\pi\rho)^{1/2}$, and we have assumed that a/L_c is small].

Thus, there are two relevant regimes—if the magnetic field is sufficiently strong, field line twist is not required for the tube to maintain its cohesion against the convective flow; however, the tube may still experience fragmentation as a result of hydrodynamic interactions resulting from its buoyant rise. In this case, a modest amount of twist can prevent the flux tube from fragmenting during its rise, and previous analyses of buoyant flux ropes in nonturbulent model convection zones are relevant (see Abbett et al. 2000, 2001). If, on the other hand, the axial magnetic field is weak compared with the kinetic energy density of the strong downdrafts, q must exceed q_c for the tube to remain cohesive, and a modest amount of twist (e.g., $q = 0.25$ along a tube of radius $a = 0.1H_r$ with $B_0 = 0.1B_{eq}$) will not provide enough additional magnetic tension for the tube to maintain its cohesion against convective turbulence.

If we apply an entropy perturbation to the tube at the onset of a simulation such that the ends of the tube are neutrally buoyant, we can simulate the evolution of a classical Ω-loop embedded in a turbulent medium. Figure 18 shows a set of such runs and demonstrates how an untwisted Ω-loop with an

initial axial field strength below the critical value ($B_0 = B_{eq}$) has its evolution dominated by convective flows, while a loop where B_0 exceeds B_c ($B_0 = 5B_{eq}$) evolves as if the convective turbulence were absent, a result consistent with the simulations presented in Paper I and those of N. H. Brummell (2002, unpublished); K. S. Cline, N. H. Brummell, & S. M. Tobias (2004, in preparation); and Cline (2003). Figure 19 shows the evolution of the same untwisted Ω-loop for a choice of $B_0 = 3B_{eq} \sim B_c$.

However, an artificial entropy perturbation is not the only computationally inexpensive way to generate Ω-loops. We find that these structures form quite naturally as a result of low-entropy downdrafts perturbing either a buoyant flux rope (see Fig. 17) or a flux layer positioned at the center of the domain (see Fig. 6, *bottom right*) or near the base (as shown in Fig. 20). In the presence of rotation, we expect loops with $B_0 > B_{eq}$ to be acted on by the Coriolis force in such a way that on average those positioned at high latitude emerge with a large tilt angle (the inclination of the leading and trailing polarities with respect to the east-west direction) and those at a low latitude emerge with a correspondingly smaller tilt angle (see Fig. 21). For $B_0 = 2B_{eq}$ (runs G1 and G2), we find that convective flows introduce a significant spread in the tilt angles of the active region progenitors that appear near the upper boundary of our simulations, although the general shape of the loops—the tendency for the trailing leg of the loop to be oriented more vertically than the leading leg (see Fig. 20)—is a feature less affected by the presence of convective turbulence.

It is important to note that we simulate the subsurface evolution of magnetic flux ropes. At the photosphere, where the acoustic Mach numbers may no longer be small and the sound speed becomes comparable to the Alfvén speed, the anelastic approximation breaks down, and a fully compressible treatment (such as that of, e.g., Tobias et al. 2001; Bercik 2002) is required. It is therefore best to think of the simulated magnetogram of Figure 21 as a snapshot of the magnetic field below the visible surface, where β is large and the anelastic treatment is valid. While our simulations seem to suggest that active regions can result from a convective perturbation of the field stored near the base of the convection zone at or near the overshoot layer, we note that observational properties of active region emergence (e.g., Hale's law and Joy's law) can be reproduced in a simulation only if a strong east-west horizontal field is imposed a priori in the lower layers at a given latitude. Further, it remains to be seen whether the strong narrow downdrafts that perturb the flux layer near the base of the simulation box will continue to penetrate to these deep layers if the Rayleigh number is substantially increased.

4. DISCUSSION

Of primary importance in determining the outcome of the simulations is the choice of initial (axial) field strength of a flux tube B_0 positioned near the bottom of the simulation domain. If the magnetic field is weak relative to the kinetic energy density of the strong downdrafts and B_0 is less than the critical value B_c of Paper I, then convection dominates the evolution of magnetic structures. In this regime, flux tubes rapidly lose their cohesion, and after several turnover times individual tubes are no longer distinguishable. Although our three-dimensional MHD models demonstrate that the local evolution of the magnetic field is complex—the tube's morphology depends on its location relative to the strong convective flows, the magnetic field is quickly swept into intergranular lanes near the surface, and the field is stretched
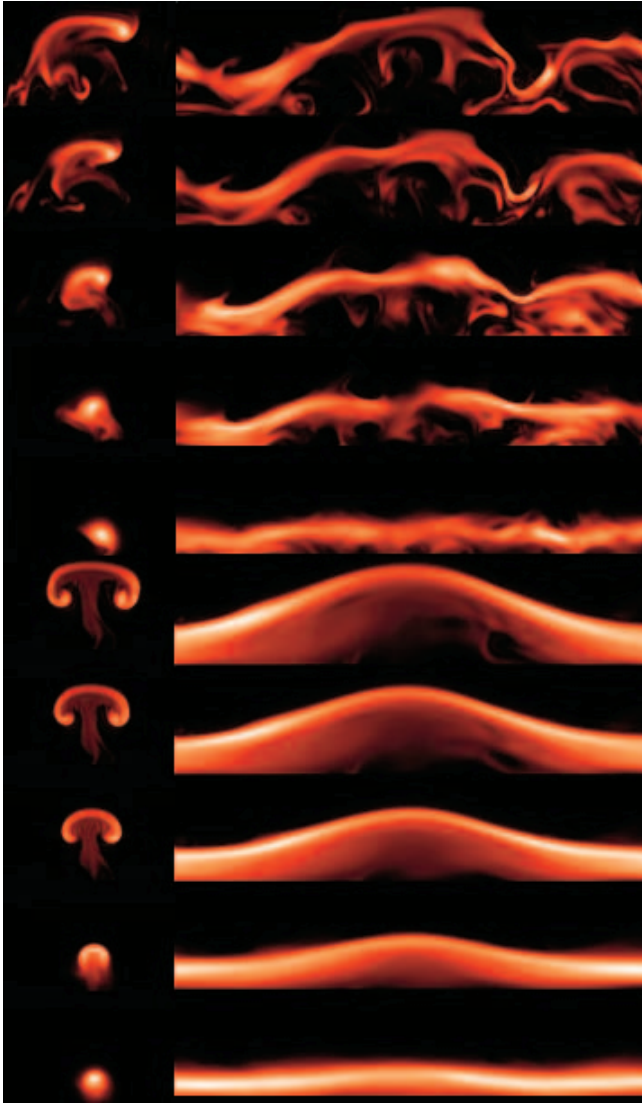
Fig. 18.—Apex cross section of $|\boldsymbol{B}|$ (*left*) as a function of height and time and a corresponding slice along the loop (*right*) for Ω-loops with no initial twist but two different values of initial field strength: $B_0 = B_{eq}$ (*top five graphs*; run D1) and $B_0 = 5B_{eq}$ (*bottom five graphs*; run D3).

Fig. 19.—Same as Fig. 18, but for an initially untwisted Ω-loop of $B_0 = 3B_{eq} \sim B_c$ (run C1).

and amplified near closed boundaries and along the narrow cool downdrafts—we find that certain global averaged quantities (such as the center of magnetic mass) evolve in a surprisingly simple manner.

If the magnetic energy of a tube or flux layer exceeds the kinetic energy density of the strong downflows, we are in a dynamic regime in which the magnetic field is no longer passively advected by convective flow; rather, the presence of the field disrupts the typical convective flow pattern. In this regime, the characteristics of the tube itself—its initial twist, the apex curvature of the Ω-loop, and its initial latitude in a rotating convection zone—determine whether or not the tube can overcome the hydrodynamic forces (independent of convective turbulence) that act to break it apart. The magnetic tension resulting from the presence of field line twist provides a force that can prevent the tube from losing its cohesion in either regime: for the case in which convective turbulence dominates the dynamics, however, the amount of twist necessary so that the tube remains intact is quite large. This is not to say that active region flux ropes must have a large amount of twist
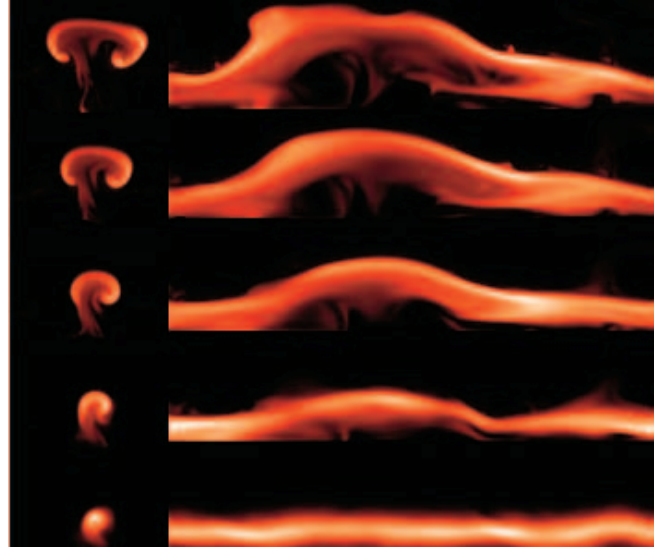
to survive their ascent through the convection zone; in fact, at field strengths typical of a large emerging active region ($B_z = 1500$ G at the photosphere), we are firmly in the regime in which the magnetic field dominates the flow, and simulations of emerging flux performed in the absence of turbulence remain relevant. Studies of this type (e.g., Abbett et al. 2000, 2001) have shown that Ω-loops embedded in a stratified (but non-turbulent) three-dimensional rotating-model convection zone require only a slight amount of field line twist to prevent fragmentation, far less than that required by completely axisymmetric tubes (see Fan et al. 1998).

We show that in the absence of systemwide background flows or oscillations in the vertical direction (i.e., $\int_0^{L_y} \int_0^{L_x} v_z \, dx \, dy = 0$ at all heights in the atmosphere), there is no initial net downward transport of magnetic flux in a closed domain given an initially horizontal magnetic structure of the form $\boldsymbol{B} = B_0 \hat{\boldsymbol{x}}$ (where $B_0 < B_{eq}$ is assumed constant), despite the presence of flow asymmetries in the vertical direction. Suppose we no longer require that density variations be small relative to the mean stratification (as can be the case in fully compressible simulations of magnetoconvection). Then we can obtain an expression for the net vertical velocity of a given layer by multiplying both sides of the equation $\rho = \overline{\rho} + \delta\rho$ (where $\delta\rho$ and $\overline{\rho}$ denote the density variations and horizontally averaged stratification) by v_z and integrating over x and y: $\int_0^{L_x} \int_0^{L_y} v_z \, dx \, dy = (1/\overline{\rho}) \int_0^{L_x} \int_0^{L_y} \rho v_z \, dx \, dy - (1/\overline{\rho}) \int_0^{L_x} \int_0^{L_y} \delta\rho v_z \, dx \, dy$.

Note that for a convectively unstable medium, when v_z is negative, $\delta\rho$ is generally greater than zero, and when v_z is positive, $\delta\rho$ is less than zero. Note also that on average for a given layer in a closed domain, $\int_0^{L_x} \int_0^{L_y} \rho v_z \, dx \, dy$ vanishes by mass conservation. Thus, if $\delta\rho$ is small (as is assumed in the anelastic approximation), we should expect that for an ensemble of numerical experiments, equation (25) holds and that there will be no initial systematic tendency for the horizontal magnetic flux layer to be preferentially transported in one vertical direction over the other solely as a result of the presence of an asymmetric vertical flow field. In a compressible medium, $\delta\rho$ may not be small, and the above argument implies that on average in convectively unstable layers, $\int_0^{L_x} \int_0^{L_y} v_z \, dx \, dy > 0$; thus, if anything, there should be a slight initial tendency for horizontal flux to be transported *upward*
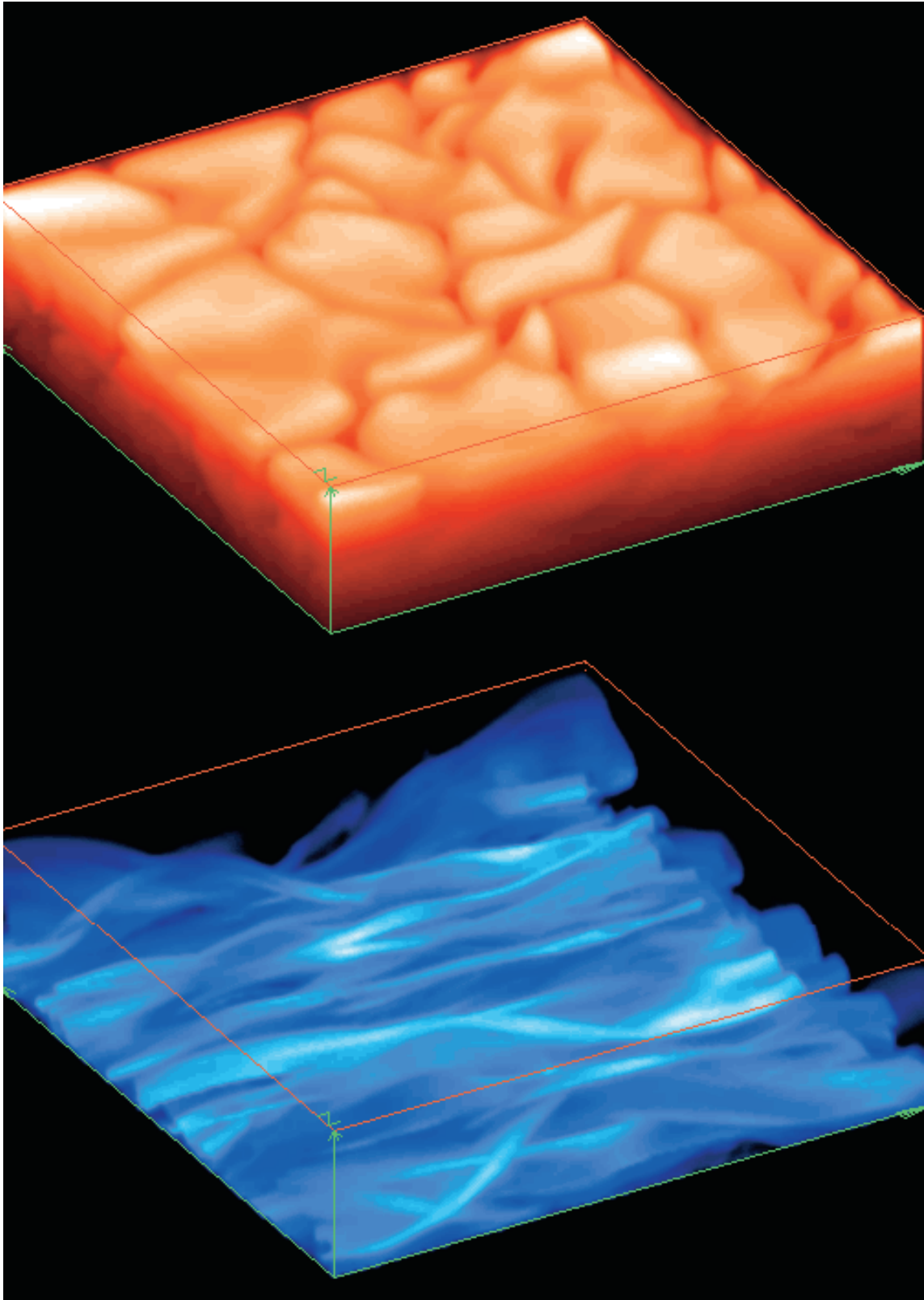
FIG. 20.—*Bottom*, Ω-loops formed from convective turbulence acting on a thin horizontal sheet of flux inserted near the base of a thermally relaxed rotating-model convection zone positioned at 15° latitude with a magnetic Rossby number of unity (run G1); *top*, corresponding volume rendering of the entropy perturbations.
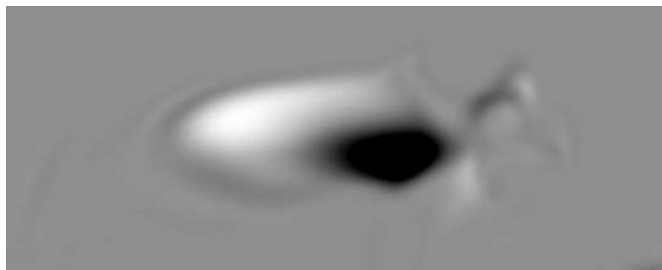
Fig. 21.—Artificial "magnetogram" (image of the vertical component of the magnetic field near the upper boundary) for one of the flux ropes formed as a result of a convective perturbation of a flux sheet positioned near the base of a rotating-model convection zone positioned at $15°$ latitude (see Fig. 20). Note that a line drawn between the leading and trailing polarities of the bipole is inclined from the horizontal (east-west) direction. The theoretical active region spans roughly 70 Mm.

toward the surface. We have tested this conjecture using data from the fully compressible simulations of surface convection performed by Bercik (2002) and have found that indeed the net vertical velocity along horizontal slices just below the visible surface (in the convectively unstable layers) is positive (although small) as the above argument predicts, while slices taken above the surface in the stable layers show a net negative vertical velocity, as one would expect.

The notion that an asymmetric flow field will preferentially transport magnetic flux in the direction of the strongest, most concentrated flows is somewhat oversimplified. While it is true that a portion of the horizontal flux layer is compressed and advected toward the base of the domain by strong localized downflows, it is also true that the vertical component of the field becomes concentrated in these circulating downflows and converging intercellular lanes (where transverse flows can tilt field lines in a manner that partially counteracts the net downward transport) and that the remainder of the flux is transported upward in broad, slower moving upflows. Rather than being correlated with the relative strength or weakness of flow asymmetries, the net vertical transport of magnetic flux through a horizontal plane (in a vertically closed domain with periodic boundary conditions in the horizontal directions) depends on whether or not there is a net component of the electric field in a direction perpendicular to both the initially horizontal flux layer and the vertical flow asymmetry, a quantity sensitive to the distribution of magnetic fields and flows on that plane. In the simulations, this occurs once the field distribution becomes significantly nonuniform, during the time when the initial magnetic layer is being expelled from cell centers into converging downflows and intergranular lanes. Once a steady state distribution is reached, there is no longer any net transport of flux into the lower half of the domain.

Thus, the robust pumping mechanism evident in MHD simulations of penetrative convection must be due to the presence of the overshoot layer. In this case, the flux entrained in the strong downflows quickly penetrates into the relatively stable overshoot region where it remains over a much longer timescale than is typical of convective turnover. Given the relative success of a diffusion model in characterizing the average properties of the flux rope of § 3.1, we suggest that a simple statistical model of diffusion, one that represents the average interaction of large-scale convective flows with smaller scale magnetic structures, may provide a useful means of interpreting global quantities obtained directly from three-dimensional MHD simulations of penetrative convection. This conjecture, in principle, can easily be tested: perform simu-

lations of magnetic flux transport in a strongly stratified convecting medium, both with and without a convective overshoot layer. If our conjecture is correct, then the addition of an overshoot layer should result in a strong turbulent pumping of magnetic flux downward, similar to that reported by, e.g., Tobias et al. (2001). Further, by changing the sub-adiabaticity of the overshoot layer, which affects the velocity and mean free path, it should be possible to change the amount of flux that can be transported downward. With our current version of ANMHD, it is not possible to add an overshoot layer, but we plan to remove this restriction in the future.

5. CONCLUSIONS

We have performed a large parameter space exploration of active region–scale magnetic flux tubes embedded in a three-dimensional stratified model convection zone to characterize the effects of convective turbulence on the subsurface evolution of an emerging magnetic structure. We summarize our principal results below:

1. If the magnetic energy density of a flux tube is weak compared with the kinetic energy density of the strong downdrafts, convective flows dominate the evolution of magnetic structures, and flux tubes of any shape quickly lose cohesion. If the initial axial field strength of a flux tube greatly exceeds the critical limit of Paper I, the tube disrupts the characteristic convective flow pattern and evolves as if the convective turbulence were absent. In this regime, the tube (or apex of an Ω-loop) may still fragment into two counterrotating elements unless either the magnetic tension due to the presence of field line twist or the effects of the Coriolis force are sufficient to suppress the hydrodynamic forces independent of convective flow that cause the tube to break apart.

2. We demonstrate that the relative strength or weakness of the vertical flow asymmetry characteristic of stratified convection is uncorrelated with the net transport of magnetic flux into the lower half of a vertically closed, horizontally periodic Cartesian domain. Given an initially horizontal, uniform magnetic field, we show that the net transport of flux across a horizontal plane can be understood in terms of the net component of the electric field along the plane normal to both the initial flux layer and the vertical flow asymmetry. We find evidence of a weak pumping mechanism once the field distribution becomes significantly nonuniform, during the time when flux from the initial magnetic layer is being expelled from cell centers into converging downflows and intergranular lanes.

3. We find that the strong pumping mechanism evident in simulations of penetrative convection—the tendency for magnetic flux to be quickly transported to the base of a stratified convection zone over multiples of a convective timescale $t_c = H_r/v_c$—does not manifest itself in a closed domain in the absence of an overshoot layer. Thus, we suggest that rapid downward transport of magnetic flux occurs as a result of the penetration of flux into the less turbulent overshoot layer where it remains for many convective turnover times, rather than simply as a result of the presence of vertical flow asymmetries.

4. Although our different treatments of the viscosity of a Newtonian fluid, in which the coefficient of either kinematic or dynamic viscosity is held constant throughout the domain, result in distinctly different model convection zones, we find that the overall evolution of embedded magnetic structures is essentially independent of the choice of model. While the detailed morphology of a given flux rope or flux layer may differ

somewhat between models, the evolution of global quantities such as the level of fragmentation of a flux tube or the position of the center of magnetic mass in the volume is insensitive to our choice of models.

REFERENCES

Abbett, W. P., Fisher, G. H., & Fan, Y. 2000, ApJ, 540, 548
———. 2001, ApJ, 546, 1194
Bercik, D. J. 2002, Ph.D. thesis, Michigan State Univ.
Brummell, N. H., Clune, T. L., & Toomre, J. 2002, ApJ, 570, 825
Brummell, N. H., Hurlburt, N. E., & Toomre, J. 1996, ApJ, 473, 494
Caligari, P., Moreno-Insertis, F., & Schüssler, M. 1995, ApJ, 441, 886
Cline, K. S. 2003, Ph.D. thesis, Univ. Colorado
Dorch, S. B. F., Gudiksen, B. V., Abbett, W. P., & Nordlund, Å. 2001, A&A, 380, 734
Dorch, S. B. F., & Nordlund, Å. 2001, A&A, 365, 562
Emonet, T., & Moreno-Insertis, F. 1998, ApJ, 492, 804
Lantz, S. R., & Fan, Y. 1999, ApJS, 121, 247
Longcope, D. W., Fisher, G. H., & Arendt, S. 1996, ApJ, 464, 999
Fan, Y. 2001, ApJ, 546, 509
Fan, Y., Abbett, W. P., & Fisher, G. H. 2003, ApJ, 582, 1206 (Paper I)
Fan, Y., & Fisher, G. H. 1996, Sol. Phys., 166, 17
Fan, Y., Zweibel, E. G., & Lantz, S. R. 1998, ApJ, 493, 480

Fan, Y., Zweibel, E. G., Linton, M. G., & Fisher, G. H. 1999, ApJ, 521, 460
Fisher, G. H., Fan, Y., & Howard, R. F. 1995, ApJ, 438, 463
Gough, D. O. 1969, J. Atmos. Sci., 26, 448
Hale, G. E., Ellerman, F., Nicholson, S. B., & Joy, A. H. 1919, ApJ, 49, 153
Linton, M. G., Longcope, D. W., & Fisher, G. H. 1996, ApJ, 469, 954
Longcope, D. W., Fisher, G. H., & Pevtsov, A. A. 1998, ApJ, 507, 417
Miesch, M. S., Brandenburg, A., & Zweibel, E. G. 2000, Phys. Rev. E, 61, 457
Ogura, Y., & Phillips, N. A. 1962, J. Atmos. Sci., 19, 173
Ossendrijver, M., Stix, M., Brandenburg, A., & Rüdiger, G. 2002, A&A, 394, 735
Spruit, H. C. 1981, A&A, 98, 155
Stein, R. F., & Nordlund, Å. 1998, ApJ, 499, 914
Tobias, S. M., Brummell, N. H., Clune, T. L., & Toomre, J. 1998, ApJ, 502, L177
———. 2001, ApJ, 549, 1183
Zirin, H. 1988, Astrophysics of the Sun (Cambridge: Cambridge Univ. Press)